12-2005

AC Loss and Thickness Dependence of Critical Currents in Coated Conductors

Anota Oluwatoyin Ijaduola
University of Tennessee - Knoxville

To the Graduate Council:

I am submitting herewith a dissertation written by Anota Oluwatoyin Ijaduola entitled "AC Loss and Thickness Dependence of Critical Currents in Coated Conductors." I have examined the final electronic copy of this dissertation for form and content and recommend that it be accepted in partial fulfillment of the requirements for the degree of Doctor of Philosophy, with a major in Physics.

J. R. Thompson, Major Professor

We have read this dissertation and recommend its acceptance:

H. H. Weitering, V. Keppens, D. K. Christen, P. Dai, C. C. Shih

Accepted for the Council:

Carolyn R. Hodges

Vice Provost and Dean of the Graduate School

(Original signatures are on file with official student records.)

To the Graduate Council:

I am submitting herewith a dissertation written by Anota Oluwatoyin Ijaduola entitled "AC Loss and Thickness Dependence of Critical Currents in Coated Conductors". I have examined the final electronic copy of this dissertation for form and content and recommend that it be accepted in partial fulfillment of the requirements for the degree of Doctor of Philosophy, with a major in Physics.

J. R. Thompson

Major Professor

We have read this dissertation
and recommend its acceptance:

H. H. Weitering

V. Keppens

D. K. Christen

P. Dai

C. C. Shih

Accepted for the Council:

Anne Mayhew

Vice Chancellor and Dean of
Graduate Studies

(Original signatures are on file with official student records.)

AC Loss and Thickness Dependence of Critical Currents in Coated Conductors

A Dissertation

Presented for the

Doctor of Philosophy

Degree

The University of Tennessee, Knoxville

Anota Oluwatoyin Ijaduola

December 2005

To the Glory of God

Allah. There is no god but He, -the Living, the Self-subsisting, Eternal. No slumber can seize Him nor sleep. His are all things in the heavens and on earth. Who is there can intercede in His presence except as He permitteth? He knoweth what (appeareth to His creatures as) before or after or behind them. Nor shall they compass aught of His knowledge except as He willeth. His Throne doth extend over the heavens and the earth, and He feeleth no fatigue in guarding and preserving them for He is the Most High, the Supreme (in glory).

Quran 2 : 255

Acknowledgments

First and foremost, my deepest gratitude goes to my advisor, Dr. James Thompson. I beleive I am not overstating the facts if I said that I have never met a more patient teacher in my life. His willingness to explain even the most trivial issues is unrivaled. His guidance throughout my studies and especially during this project has allowed me to develop my skills as a researcher within a supportive team environment. I thank him for the opportunity.

Also, I would like to thank the other members of my committee: Drs. Hanno Weitering, Pengcheng Dai, Chia Shih, Veerle Keppens, and David Christen. Your time, guidance and input into this dissertation is greatly appreciated.

Many thanks also go to my collaborators at ORNL, AMSC and Oxford Instruments. Dr. Feenstra made all the YBCO samples used in the thickness dependency studies. Drs. Goyal, Thieme and Marken provided the Ni-W textured substrates. The TEM images were taken by Dr. Song at the University of Wisconsin, Madison.

My building mates at the ORNL have been wonderful to me since I joined the group. First, special thanks to Dr. David Christen who is the head of the superconductivity group and also served on my committee. His timely advice and suggestions have helped enormously. Tolga Aytug, Albert Gapud, Claudia Cantoni, Yifei Zhang and Nancy Ward are great friends and colleagues.

To my fellow graduate students, I express my gratitude for the many conversations that have had a tremendous impact on my research and myself as a person. Valentina, Maria, Hye-Jung, Tom, Jason, Victor, and others too numerous to mention, thank you very much.

I must express my appreciation to the many friends outside of my studies who have helped to relieve the sometimes stressful solitude of graduate school. Dr. and Mrs. Badiru are wonderful "parents" and "grandparents" to me and my son. Femi and Remi Omitaomu are my *confidantes*; Muyiwa and Helen Asaolu are great friends. Bukky Ojemakinde (Mrs. OJ), Godswill Nsofor (Doc), Ruby, Dapo, Funmi, Funke, Oreoluwa, Ibukun, Kemi, and Tayo are like brothers and sisters to me. May the Almighty God continue to bless you and all that is yours. *Gbogbo wa ni a maa ko ere oko de ile o (Amin).*

I am deeply indebted to my family, especially my parents, Arashi and Falilat Lawal. To my siblings: Tosin, Nurat, Kamil, Kasirat and Morufat, thanks for holding forth at home. I also owe a special thanks to my Uncle, Mr. Sola Lawal. He has always been a source of inspiration to me.

It is one thing to have a great family, but it is a blessing to have a wonderful spouse. My sincerest gratitude goes to my husband, Dr. Razaq Ijaduola. Words cannot express how thankful I am to have you. Where I am today is in no small part due to your love and support. *Ose pupo o Ajao Okin mi.* May Almighty Allah continue to strengthen our love and commitments to each other. And to my son, Ibrahim Ijaduola (Ishola), thanks for the joy you have brought to our lives.

Lastly and most importantly, all thanks to Almighty Allah, the Beneficient, the Merciful. None deserves the glory but You o Lord. **ALHAMDULILLAH**.

Abstract

This program of research is directed toward understanding the physical properties of certain materials in superconductive "coated conductors." Specifically investigated were $Ni_{1-x}W_x$ alloys for use as substrate and thin films of $YBa_2Cu_3O_7$, a high- T_c superconductor with many attractive features.

A study has been conducted on the magnetic properties of a series of biaxially textured $Ni_{1-x}W_x$ materials with compositions x = 0, 3, 5, 6, and 9 at.% W. These materials are important as substrates for "RABiTS"-type coated conductors that incorporate high temperature superconductors for current transport. The quasi-static dc and ac hysteretic loss W was determined to support estimates of the ferromagnetic contribution to the overall ac loss in potential ac applications. The alloys were prepared by either vacuum casting or powder metallurgy methods, and the hysteretic loss tended to be lower in materials that were recrystallized at higher temperatures. Some samples were progressively deformed to simulate winding operations; this increased the hysteretic loss, as did sample cutting operations that create localized damage. In ac magnetization measurements, the effects of ac frequency and dc bias field on the ferromagnetic loss were determined.

Furthermore, in order to better understand the complex problem of vortex pinning and the identification of defects that support the critical current density J_c in these "RABiTS"-type coated conductors, we have made magnetometric studies of the J_c flowing in thin $YBa_2Cu_3O_{7-d}$ (YBCO) films of various thicknesses d, both as a function of applied field H and temperature T. The films, grown by a BaF_2 *ex - situ* process and deposited

on buffered"RABiTS" substrates of Ni-5%W, have thicknesses d ranging from 28 nm to 1.5 μm.

Isothermal magnetization loops $M(H;T)$ and remanent magnetization $M_{rem}(T)$ in zero applied field $H = 0$, were measured with H $\|$ c-axis (i.e., normal to film plane). The $J_c(d)$ values, which were obtained from a modified critical state model, increase with thickness d, peak near a particular thickness, and thereafter decrease as the films get thicker. For a wide range of temperatures and intermediate fields, we find a power law falloff $J_c \propto H^{-\beta}$ with $\beta \sim$ (0.56 - 0.69) for all materials. This feature compares well with the power-law exponent $\beta = 5/8$ obtained theoretically by Ovchinnikov and Ivlev for pinning by large random defects, as are observed by TEM. Comparison of the theoretical predictions with experimental $J_c(H, T, d)$ yields a mostly consistent picture, using values for the size and density of defects that are comparable with those deduced from TEM images.

Finally, for higher temperatures approaching the irreversibility line, we find $J_c(T, sf) \propto (1 - T/T_c)^n$ with n $\sim$ 1.1 - 1.3. This points to "δT_c *pinning*" (pinning that suppresses T_c locally) in all of these YBCO materials, as expected for the observed large, non-superconducting defects.

Contents

List of Figures

List of Symbols and Abbreviations

a	plane separation in XRD
A	magnetic vector potential
ac	alternating current
AMSC	American Superconductor Corporation
B, $\mathbf{B}$	(scalar, vector) magnetic induction
c	speed of light
C_{66}	elastic shear modulus
C_{44}	elastic tilt modulus
d	film thickness
D_z^i	defect size along field direction
D_i	defect size along the other directions
dc	direct current
e	charge of an electron
f	frequency
F_p, f_p^i	pinning force
FM	Ferromagnet/ Ferromagnetism
g	Landé factor
h	Planck's constant
H, $\mathbf{H}$	(scalar, vector) magnetic field strength
h_{ac}	ac field amplitude
H_c	thermodynamic critical field

H_{dc}	dc bias field
H_{c1}	first (lower) critical field
H_{c2}	second (higher) critical field
H_{max}	maximum field
HTS or HTSC	High Temperature Superconduct(or)ivity
I_c	critical current
I_0, I_p	peak ac current
IBAD	Ion Beam Assisted Deposition
ISD	Inclined Substrate Deposition
J	current density
J_0	depairing current density
J_c	critical current density
J_{ij}	exchange integrals
K_B, k	Boltzmann constant
L_c, R_c	correlation length (longitudinal, transverse)
m, $\mathbf{m}$	(scalar, vector) magnetic moment
M	magnetization/ mass magnetization
M'	in phase mass magnetization
M''	out-of-phase mass magnetization
M_{rem}	remanent magnetization
MPMS	Magnetic Property Measuring System
n_i, n_s	number density
ORNL	Oak Ridge National Laboratory
PIT	Powder In Tube
PM	Powder Metallurgy
PVD	Physical Vapor Deposition
QCM	Quartz Crystal Monitors
RABiTS	Rolling Assisted Biaxially Textured Substrates
RBS	Rutherford Backscattering Spectroscopy

S_i, $\mathbf{S_i}$	spin
SC	Superconductor
SQuID	Superconducting Quantum Interference Device
T_c	critical or Curie temperature
T	temperature
TEM	Transmission Electron Microscopy
U_p	pinning energy
V_c	correlation volume
VC	Vacuum Cast
w	width of tape
W	loss/cycle
x	nominal composition of W in Ni
XRD	X-Ray Diffraction
ϵ	anisotropy parameter
ϵ_0 / ϵ_1	energy per unit length / vortex line energy
κ	Ginzburg - Landau (GL) constant
λ	penetration depth
μ_0	permeability in free space
μ_B	Bohr magneton
ξ	coherence length
σ	specific magnetization
Φ_0	flux quantum
χ	susceptibility
ψ	wave function

Chapter 1

Introduction

Superconductivity was discovered in 1911 by H. Kamerlingh Onnes [1] in Leiden, Netherlands, just three years after he had liquefied helium, giving him the refrigeration technique required to reach temperatures of a few degrees Kelvin. The first superconductors discovered, which were elements, alloys, and compounds, have very low critical temperatures, T_c often in the range of 1-20 K. For example, the first superconductor discovered was mercury with a T_c of 4 K. These are the so called low temperature superconductors. Then, in 1986, J. G. Bednorz and K. A. Muller, working at the IBM Research Laboratory in Zurich, Switzerland, found a material La_2CuO_4 with T_c in excess of 30 K [2]. This was the beginning era of the high temperature superconductor(HTSC). What followed this discovery was an unprecedented worldwide outburst of excitement and activity in this field. It was no surprise then that another cuprate (copper oxide) compound $YBa_2Cu_3O_{7-\delta}$ (YBCO) with a T_c of about 90 K was discovered in the following year [3]. Soon after their discovery, the quest for practical applications led to investigations on the current carrying capacity of this material.

This quest to make HTSC more technologically relevant led to the idea of coated conductors. A big problem of low critical current density J_c due to the improper alignment of the grain is circumvented by depositing the superconducting films on well textured substrates. One of the methods used for this is the Rolling Assisted Biaxially Textured Substrates (RABiTS) These substrates, being ferromagnetic (FM), contribute to the overall ac loss in

the coated conductor. In this work, we have studied extensively the magnetic properties and ferromagnetic loss of Ni-W alloys used as substrates for YBCO based materials. Also, we have shown and explained factors that contibute to their being lossy.

When conducting currents, HTSC material generally is immersed in a magnetic field, which arises from its own currents or external fields (or both). This causes magnetic flux to enter, in the form of vortices which are quantized. The effect of magnetic relaxation in HTSC arise due to the motion of vortices. In order to have high values of J_c, vortices have to be well pinned, i.e., made immobile. Understanding the physics of vortices can help in explaining the thickness dependence of J_c in the YBCO films. The relationship between the J_c and the applied field can give an insight into the type of vortex pinning in superconductors. By comparing experimental results with theoretical predictions, we can identify the dominant pinning mechanisms in these materials. Furthermore, from the thickness dependence studies of the J_c, we should be able to determine if we can get very high overall J_c from making stack of thin films each with individually high J_c. In the second part of this work, we have studied how the J_c in thin YBCO films deposited on Ni-5%W RABiTS substrates depends on the film thickness, the applied magnetic field and temperature. This was done in order to understand more the nature of the pinning mechanisms and vortex structure in these types of materials.

The remaining part of this chapter gives a broad introduction to the different aspects of the entailing subjects in this work. Chapter 2 deals with the theoretical background while Chapter 3 explains the experimental details and set up. The results obtained are collected in Chapter 4 and we conclude and give possible future directions in Chapter 5.

1.1 Coated Conductors

The so-called first generation HTSC wires were polycrystalline bulk BSCCO (Bi-Sr-Ca-Cu-O) and YBCO samples, which were rather disappointing due to their low current capability, especially in a magnetic field. The first generation superconducting wires depend on the easy cleavage of the double Bi-O layer of the Bi2212 phases for the texture formation.

But problems of low J_c especially across large angle grain boundaries still persisted. The most common fabrication process used then is the powder-in-tube (PIT) process [4]. The material of choice for the tube is silver or a silver alloy. Silver is permeable to oxygen, is nonreactive with the HTS core material, lowers the melting point of Bi-based HTS materials during thermal processing, and forms a template upon which the HTS material can grow. Typically, the tube is filled with HTS powder, then extruded or drawn to wire about 1-2 mm in diameter. For multifilament conductor, the wire is drawn in a hexagonal shape, cut into shorter lengths, and formed into a stack of numbers of filaments. This stack is then inserted in another tube, and the composite is extruded or drawn to wire. (See Figs. 1.1 for schematic representations).

In the second generation wires, the coated conductors (CC), the problem of low current conduction across grain boundaries was resolved in part by properly texturing of the HTSC films. Among the various HTSC materials, YBCO attracts the most attention because of its current carrying ability in a magnetic field and high current density in self-field. While the sintered polycrystalline bulk YBCO was rather disappointing for its limited current carrying capacity especially in a magnetic field, well textured YBCO films showed much greater potential for practical applications [5]. Moreover, compared with the BSCCO first generation HTSC wire, YBCO is less anisotropic and has much higher J_c in magnetic fields at elevated temperatures, which is crucial to many applications. The success of HTSC film deposition on small single crystal substrates led to the idea of a coated conductor, so-called second generation HTSC wire. Presently, HTSC films are deposited on flexible metallic tapes using different techniques for making well textured substrates and superconducting layers. The most common techniques are RABiTS (Rolling Assisted Biaxially Textured Substrates) [6,7,8], IBAD (Ion Beam Assisted Deposition) [9,10] and ISD (Inclined Substrate Deposition) [11,12]. All of these techniques have become possible candidates for being scaled up for industrial applications.

One of the chief obstacles to the manufacture of commercial lengths of these YBCO wire has been the phenomenon of weak links, which exist where current crosses a structural discontinuity such as a grain boundary. This weak inter-grain coupling manifests itself as

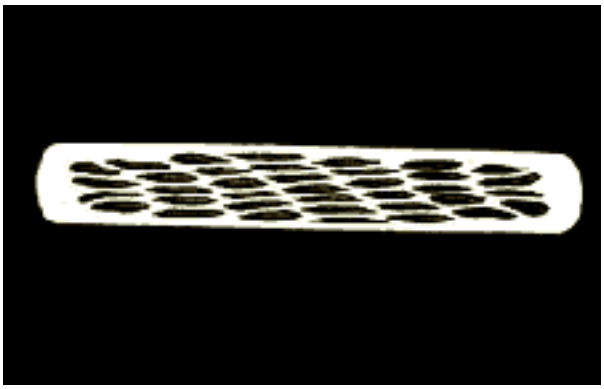

(a)

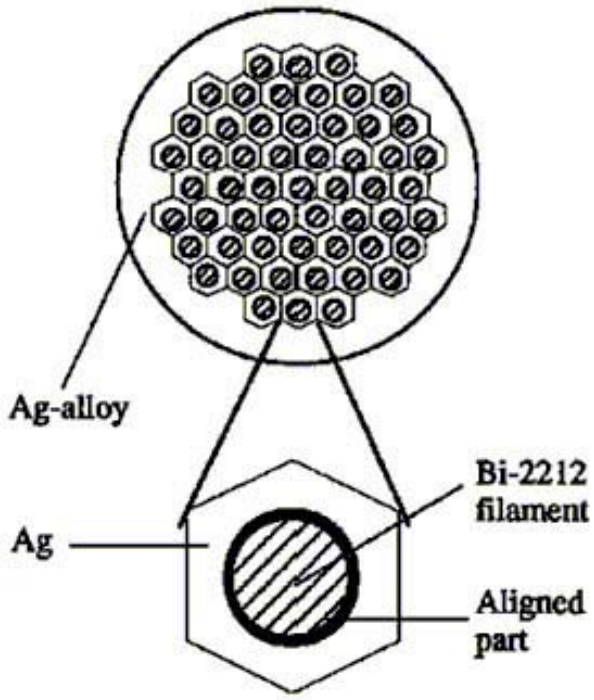

(b)

Figure 1.1: (a) Schematic diagram of a BSCCO PIT wire. (b) Transverse section of the wire showing the BSCCO filament core, the inner Ag sheath with well textured material at the core/Ag interface, and the outer Ag - alloy sheath for high strength.

an inability of the material to transport a significant supercurrent density from grain to grain, even though the current transport within individual grains can be quite good. By aligning grains carefully, low angle boundaries between superconducting grains are assured, which allows more current to flow.

The RABiTS method achieves this alignment by producing high quality biaxial texture in a range of materials, including metals, and certain oxides deposited epitaxially on a textured metal strip. These textured substrates serve as structural templates for the final superconducting layer, which has substantially fewer weak links. The three main steps of the RABiTS process are biaxially textured metal fabrication, buffer layer deposition, and superconductor deposition. The base metal of choice now is nickel or its alloys, which is first roll-textured and heat-treated. Next, extremely thin layers of ceramic materials called buffer layers are rapidly deposited using an electron beam or sputtering system before the final deposition of the superconducting layer. The buffer layer is necessary to provide a chemical barrier between the Ni alloy and the YBCO superconducting layer while maintaining the texture, retarding NiO formation and aiding lattice matching between the substrate and YBCO. Examples of buffer layers used are CeO_2, YSZ, Re_2O_3 and TMO [transition metal oxides]. Fig. 1.2 shows the architecture of a coated conductor while Fig. 1.3 summarises the main processes involved in the RABiTs process.

1.2 AC Loss

Although a superconductor can in principle carry a dc current without resistance, an ac current or a changing magnetic field will lead to losses. (The origin of the loss is a hysteresis). It is the irreversibility in the increasing and the decreasing applied magnetic field that is reponsible for this hysteresis. For these coated conductors, ac loss arises from the superconductors themselves and from the metallic substrates. We need to study these losses to understand them and devise ways to reduce, if not totally eliminate them.

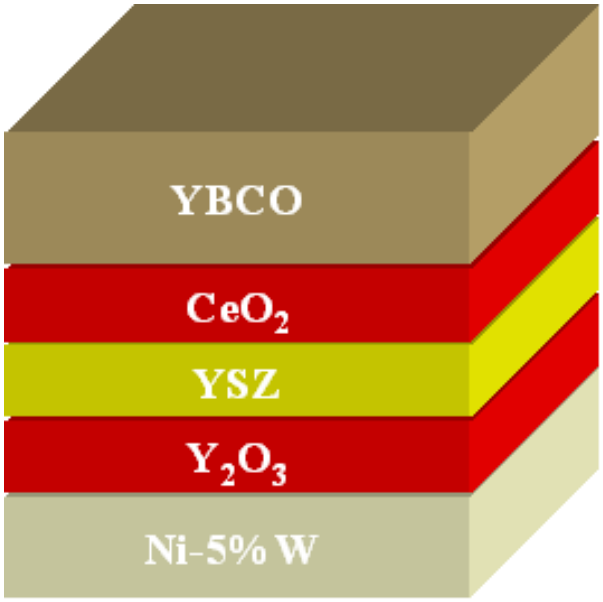

Figure 1.2: The architecture of a coated conductor. Here, Ni5%W is the ferromagnetic substrate.

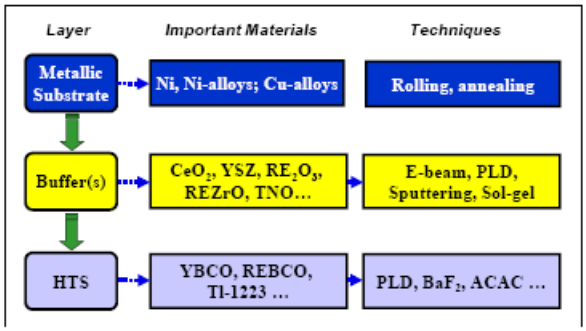

Figure 1.3: The three main steps involved in the RABiTS process.

The ac loss is of interest because the losses occur at low temperatures, meaning that a large amount of refrigeration power is required to remove the heat. Hence the ac loss must be kept at the barest minimum. AC losses for the coated conductor geometry studied in this work come primarily from three sources. First is the hysteretic loss in the superconductor itself. A superconductor can acquire resistance due to the excitation of normal electrons across an energy gap (aided by relatively high temperature in the HTSC). At low frequencies, resistance arises because of flux flow and flux creep. In general, HTSC are subject to losses because electric fields can be produced inside it. In many applications the electric field results from applying a transverse alternating magnetic field, and the loss it produces is called the transverse applied field loss. This loss is a form of hysteresis loss. It is generated by the penetration of the self-field from the applied ac current and can be measured experimentally by numerically integrating the $M(H)$ loop obtained from magnetization measurement to obtain its area.

The second contribution to the ac loss comes from ferromagnetic (FM) hysteretic in the alloy substrate, which is driven by the fields generated by the ac currents. Metallic substrates with non-magnetic or minimum magnetic hysteretic loss are preferred. Because of their good texturing properties and resistance to oxidation, however, Ni and its alloys are commonly used, although research is ongoing to introduce even lesser ferromagnetic or nonmagnetic alloys like copper based alloys [13]. We have studied extensively the magnetic properties and FM losses of Ni-Cr alloys [14] and Ni-W alloys [15]. From our measurements, we found that the fraction of the FM loss of the total ac loss becomes progressively larger as I_p gets smaller, i.e. for lower current levels. When subjected to shearing or bending deformation (as might be caused by winding or bending of conductors), Ni-W alloys gave higher levels of FM loss and also, alloys that are re-crystallised at lower temperatures tend to be more lossy. Underlying these observations is the fact that the FM loss arises from movement of magnetic domains in the substrate, which is itself a soft FM material. Thus any mechanism that tends to increase domain wall pinning (work hardening, etc) increases the ac loss.

Lastly, the third form of ac loss is due to the eddy currents that are generated in the substrate which give rise to eddy loss. This is negligible in our case due to the large size of the skin depth of our alloys compared to their thicknesses.

1.3 Vortex Behavior and J_c in HTSC

All HTSC materials are type II superconductors. This means that in magnetic field $H_{c1} < H < H_{c2}$, which is the range of fields typically required for most applications, they are in the mixed/vortex state. In this state, magnetic fields penetrate them in a regular array of flux tubes, each carrying a quantum of flux $\phi_0 = h/2e$. A tube of material is called a vortex and at its center the superconducting order parameter ψ reaches zero. The current circulating around a vortex makes each vortex act like a tiny bar magnet. These vortices repel each other because the currents circulating about one vortex produce a repulsive Lorentz force, $\mathbf{J} \times \mathbf{B}$, on the magnetic field of another vortex. In an external magnetic field, this force can and does move the vortices, thereby creating a longitudinal potential gradient parallel to the transport current. This is equivalent to a power loss or a dissipation in the material. Thus, when vortices move under the influence of a transport current, energy is dissipated and the material has a resistive loss. Fig. 1.4 is a cartoon illustration of this phenomenom.

Resistance-less operation can be achieved only if the vortices are strongly pinned. To pin vortices, potential wells must be created in which the vortex has a lower energy than in its surroundings. Thus, the vortex 'sits' at a pinning site. If the potential well is very

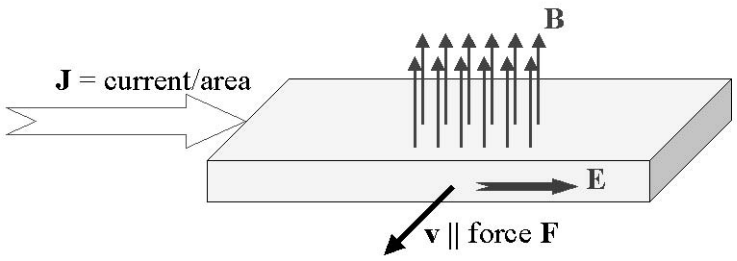

Figure 1.4: Motion of vortices in a superconductor. $F = J \times B$; If vortices move at velocity v, then there exists electric field $E = B \times v$ with $E \| J$.

deep, neither the Lorentz force nor thermal energy will be able to move the vortex. Pinning results from spatial inhomogeneities of the material, such as impurities, grain boundaries, voids, dislocations and oxygen vacancies in the structure of the cuprates. Pinning at these types of sites occurs because it costs less energy if the vortex core is at a position that is normal, than if it must change a superconducting region to a normal region. To produce magnetic pinning, the inhomogeneities may be on the scale of λ where λ is the penetration depth. For HTSC, the more important situation is vortex-core pinning, in which case the inhomogeneities should be on the scale of the coherence length ξ. The very small ξ values allows for pinning to be accomplished by atomic defects, especially if the defects are on the Cu-O planes.

In addition to the intrinsic or naturally occurring pinning, different methods exist by which vortices can be pinned in energetically favorable locations. One such methods is the "artificial" post-growth treatment of the film by irradiation with energetic heavy ions [16] (which can produce columnar defects). More recently, another scheme was introduced [17]. This involves introducing defects in the YBCO films during growth. These defects are nanoparticles of $BaZrO_3$ grown heteroepitaxially within laser-ablated YBCO films.

The critical current density J_c (current per cross-sectional area through which it flows) is a major electrical parameter of a superconductor's performance. It is the maximum current density that can be sustained by a superconductor before significant dissipation develops. (That there must be some upper limit to the current density is required by the relationship between current and magnetic field). There are various ways by which J_c can be estimated in a superconductor. In this work, we will use magnetization measurements. This magnetometric study is based on a simple equation from electrodynamics which relates the magnetic dipole moment generated by the circulating current. Further discussion of this is in the chapter on theoretical aspects.

Chapter 2

Theoretical Aspects

The RABiTS [6, 7, 8] technique uses standard thermomechanical processing to obtain long lengths of flexible, biaxially oriented substrates with smooth surfaces. The strong biaxial texture of the base metal is conferred to the superconductor by the deposition of intermediate metal and/or oxide layers that serve both as a chemical and a structural buffer. Because of their good texturing properties and resistance to oxidation, nickel and its alloys are commonly used. Ni has a structure of face-centered cubic at all temperatures (See Fig. 2.1). It forms strong cube texture following heavy cold rolling and recrystallization which is one of the reasons why it is widely used as a RABiTS substrates. But problems arising from its high ferromagnetism such as significant hystereric losses make it necessary to develop suitable alloys to replace it as the base material for RABiTS coated conductors. A common RABiTS architecture looks like this: YBCO/CeO2/YSZ/Y2O3/Ni-W alloy.

In this chapter, the theoretical background needed for the work will be developed. The first section will cover the Weiss theory of ferromagnetism, which explains the ferromagnetic properties of Ni and by extension, of Ni-W whose phase diagram is shown in Fig. 2.2. Section 2.2 will give details on vortices and pinning mechanisms in superconductors. Here, topics such as the relevant energy and length scales and theoretical models of pinning mechanisms will be presented. Also, the Bean critical state model will be described.

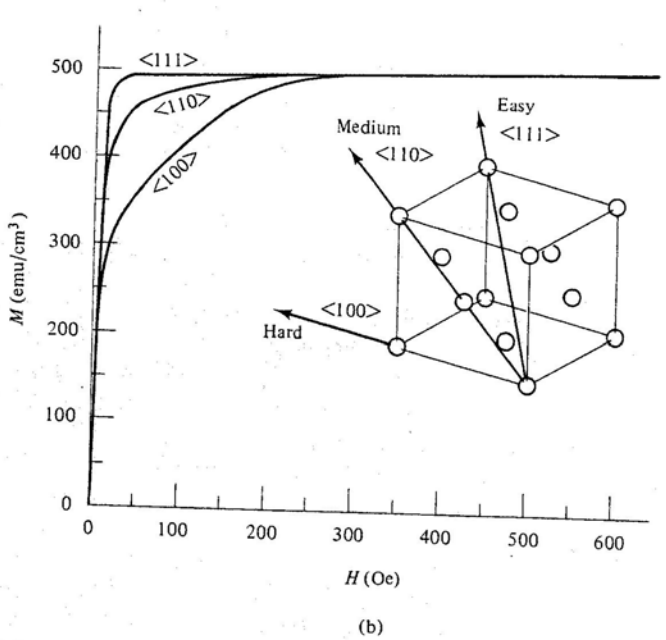

Figure 2.1: The crystalline structure of fcc Ni. The magnetic response in different crystal directions is also shown. (Figure from Cullity.)

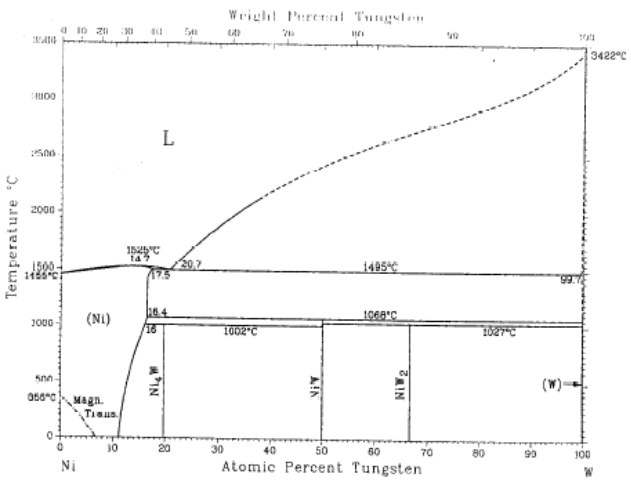

Figure 2.2: The phase diagram of Ni-W.

The last section will focus on the ac loss on superconductors with emphasis on the theory of Norris [18] which provides a reasonably good description of the superconductive portion of the ac loss in these materials.

2.1 Weiss Theory of Ferromagnetism

Nickel is one of the three of the $3d$ transition metals with high Curie points and spontaneous magnetizations at room temperature; its other ferromagnetic partners are iron and cobalt. The carriers of the magnetism, the $3d$ electrons, are located relatively far from the atomic core, and are considered to be moving among the atoms, rather than localized at individual atoms. In other words, they form a band structure. The origin of this strong magnetism is the presence of a spontaneous magnetization produced by a parallel alignment of the spins.

The mechanism for the apperance of spontaneous magnetization was first clarified by P. Weiss [19] in 1907. He assumed that in a ferromagnetic material there exists an effective field which was considered to align the neighboring spins parallel to one another. These spins interact with each other, each of them trying to align the others in its own direction. This interaction between them originates from the quantum mechanical properties of spins and it can be expressed as an *exchange energy* between spin $\mathbf{S}_i$ and spin $\mathbf{S}_j$, which is proportional to $\mathbf{S}_i \cdot \mathbf{S}_j$

Including the same energy of interaction with an applied field, $\mathbf{H}$, the total energy of a system is thus

$$E = -\sum_{i \neq j} J_{ij} \mathbf{S}_i \cdot \mathbf{S}_j - \sum_i g\mu_B \mathbf{S}_i \cdot \mathbf{H}, \tag{2.1}$$

The coefficients J_{ij} are called the exchange integrals and their signs are defined so that if J_{ij} is positive, parallel spins have a lower energy than antiparallel ones, which is the case for a ferromagnetic interaction. The magnitude m of the moment $\mathbf{m}$ is $g\mu_B S$ where g is the so-called Landé factor and μ_B is the Bohr magneton.

Very many bodies are involved, and some approximation is inevitable. Here, we will use the *molecular/mean field approximation*. In this method, one spin is tagged for checking its statistics in more detail, while the others are just replaced by their mean value. Then after some manipulations, that particular spin is *untagged*, saying that on the average it is not any different from the other spins thus obtaining the mean value.

Specifically, we consider the spin $\mathbf{S}_i$ as something special, and collect together the energy terms in which it is involved when all the other spins, $\mathbf{S}_j$, are replaced by their mean value, $\langle \mathbf{S}_j \rangle$,

$$E_i = -2 \sum_j J_{ij} \mathbf{S}_i \cdot \langle \mathbf{S}_j \rangle - g\mu_B \mathbf{S}_i \cdot \mathbf{H} = -\mathbf{S}_i \cdot \mathbf{H}_i, \tag{2.2}$$

where

$$\mathbf{H}_i = g\mu_B \mathbf{H} + 2 \sum_j J_{ij} \langle \mathbf{S}_j \rangle . \tag{2.3}$$

To the present approximation, the exchange interaction between the spins has thus turned out to be equivalent to an interaction of each spin with an effective field, $\mathbf{H}_i$, which is non-zero even when the real applied field $\mathbf{H}$ vanishes. This is essentially the assumption of Weiss.

The problem of ferromagnetism has thus been reduced to the problem of isolated spins interacting with an applied field. Solving Eq. 2.2, the z-component of $\mathbf{S}_i$ becomes

$$\langle \mathbf{S}_{iz} \rangle = S B_s \left(\frac{S H_i}{k_B T} \right), \tag{2.4}$$

where H_i is defined in Eq. 2.3 and B_s is the Brillouin function which depends on both the argument and the spin number, S. Substituting Eq. 2.3 into Eq. 2.4 and suppressing the index i yields,

$$\langle S_z \rangle = S B_s \left(\frac{S}{k_B T} \left[g\mu_B H + 2 \langle S_z \rangle \sum_j J_{ij}, \right] \right) \tag{2.5}$$

which is a transcendental equation for determining $\langle S_z \rangle$

With a modern computer a numerical solution of Eq. 2.5 is a trivial matter and for a small value of H, the solution looks like the plot in Fig. 2.3 for nickel.

Furthermore, the solution of Eq. 2.5 is zero in zero applied field for any temperature above a transition point, namely the Curie point. In this region of $T > T_c$, it is known from experiment that all ferromagnets become regular paramagnets. It is also clear that for a sufficiently high temperature the thermal fluctuations overcome the exchange interaction between the spins, thus eliminating the ferromagnetic *order* and making the material as disordered as a paramagnet. A quantitative study of Eq. 2.5 in the high temperature region where it is sufficient to approximate the Brillouin function by the first term of a power series expansion, yield the famous *Curie-Weiss law* [20]:

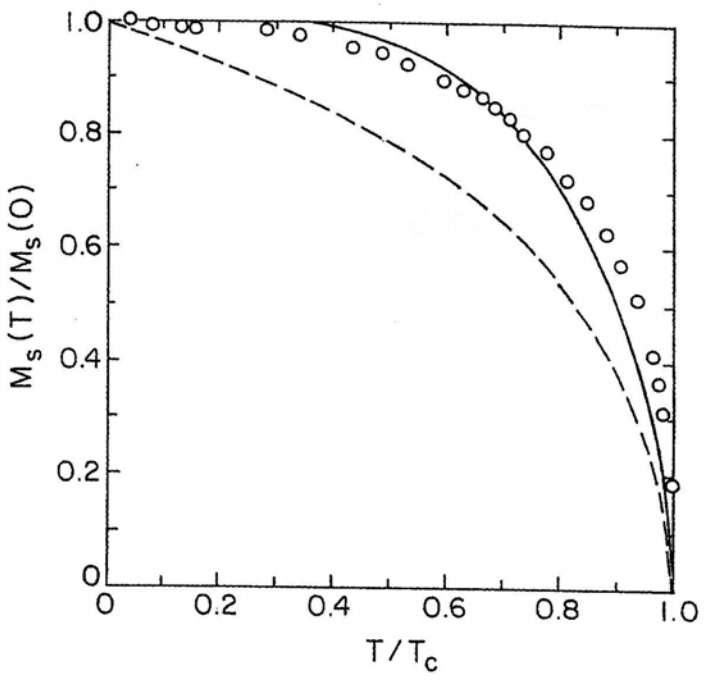

Figure 2.3: Reduced magnetization versus reduced temperature for nickel. Solid line is the Brillouin function for $S = 1/2$ and the dashed line is the classical solution for $S = \infty$. This is an approximate shape of the solution of Eq. 2.5. (Figure from O'Handley.)

$$\langle M_z \rangle = g\mu_B \langle S_{total} \rangle = \frac{CH}{T - \Theta} \tag{2.6}$$

where

$$C = \frac{2S(S+1)}{3k_B}(g\mu_B)^2, \tag{2.7}$$

and

$$\Theta = T_c = \frac{2S(S+1)}{3k_B}(pJ) \tag{2.8}$$

p is the number of nearest neighbor and J is the ferromagnetic coupling.

Eq. 2.6 is more usually expressed in terms of the initial susceptibility,

$$\chi_{initial} = \underbrace{Lim}_{H \to 0} \frac{\langle M_z \rangle}{H} = \frac{C}{T - \Theta} \tag{2.9}$$

This means that χ will diverge at $T = T_c$. T_c is the temperature that separates the ordered state, where the internal field dominates the thermal effect, from the disordered state where thermal disorder reigns.

Also in all ferromagnetic materials, the magnetic moments of the individual atoms **m** interact strongly with each other. This interaction creates a certain degree of macroscopic order below T_c even in the absence of an applied field. This order is the cause of a non-zero average magnetic moment in zero field. Actually, **m** is typically not even a single-valued function of the magnetic field **H**, and its value depends on the history of the applied field. A typical case in shown in Fig. 2.4 which plots the component of **M** as a function of the magnitude of the field. **M** is the moment per volume or *magnetization* and this type of plot is referred to as a *hysteresis loop*. As the applied field gets larger, more spins align with the magnetic field until such a point that all spins are aligned. The system has then reached *saturation magnetization* $\mathbf{M_s}$. As the field is reduced, spins lose their alignment and **M** decreases. At **H**=0, a ferromagnet will have residual magnetization, called *remanent magnetization* or *remanence* $\mathbf{M_r}$. To remove the magnetization, a reverse field called the

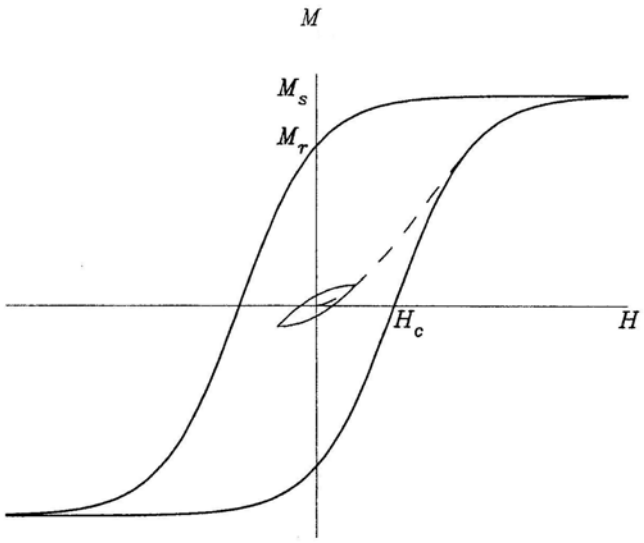

Figure 2.4: Hysteresis loop of a typical ferromagnet. Also displayed are the virgin curve (dashed), and one minor loop. The remanence, M_r, the saturation magnetization, M_s and the coercivity, H_c are as indicated. (Figure from Aharoni.)

coercive field $\mathbf{H_c}$ must be applied. The area of a hysteresis loop is related to the energy dissipated every time the magnetization is taken around the loop.

In principle, any theory of ferromagnetism should address both of these phenomena. It should thus explain the hysteresis displayed in Fig. 2.4 and the temperature dependence of Eq. 2.5 as shown in Fig. 2.3.

Qualitatively, both phenomena are understood to a certain extent due to an explanation given by Weiss [19]. He assumed that there is a certain internal or "molecular" field in ferromagnetic materials as outlined earlier, which is responsible for the temperature dependence displayed in Eq. 2.9. In order to explain the unusual field dependence in Fig. 2.4, Weiss assumed that ferromagnets are made out of many *domains*. Each of these domains is magnetized to the saturation value $M_s(T)$, but the *direction* of the magnetization vector varies from one domain to the other. Domains are separated from one another by 'domain walls'. At domain boundaries there are transition layers where spins gradually change their direction from one domain to the other. These transition layers are called *domain walls* (See Fig. 2.5). The measured value of the magnetization is the average over these domains,

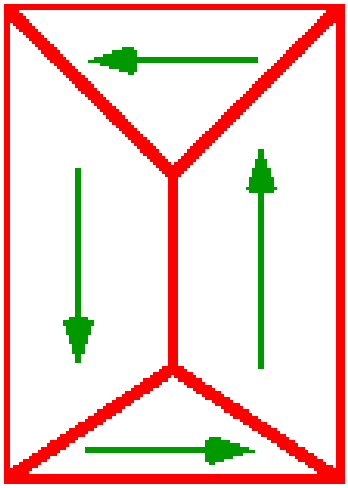

Figure 2.5: Magnetic domains in a ferromagnetic material. Each domain is separated by a domain wall.

which can be zero in any particular direction where there is an equal number of domains parallel and antiparallel to that direction. It can also have a non-zero value, numerically less than $M_s(T)$, if this number of domains is not equal. The applied magnetic field rotates the magnetization of the individual domains into its own direction, and when this field is sufficiently large to align all domains, the measured average becomes $M_s(T)$. Fig. 2.6 illustrates this phenomenon.

2.2 Physics of Superconductors

2.2.1 The London Equations

A superconductor, when cooled below its T_c in a magnetic field, expels all its magnetic flux ideally. Thus, in a weak magnetic field, a superconductor has *perfect diamagnetism*, a phenomenom called the *Meissner effect* [21]. Perfect diamagnetism is completely different from what one would expect in a metal with infinite conductivity, which when cooled in a magnetic field, would trap the magnetic flux in the conductor. The Meissner effect implies that in a magnetic field, superconductors develop surface current, which give rise to magnetic fields that exactly cancel the external field, leaving a field-free bulk. The Meissner effect also implies a *critical field*, H_c, above which superconductivity will be destroyed. The London

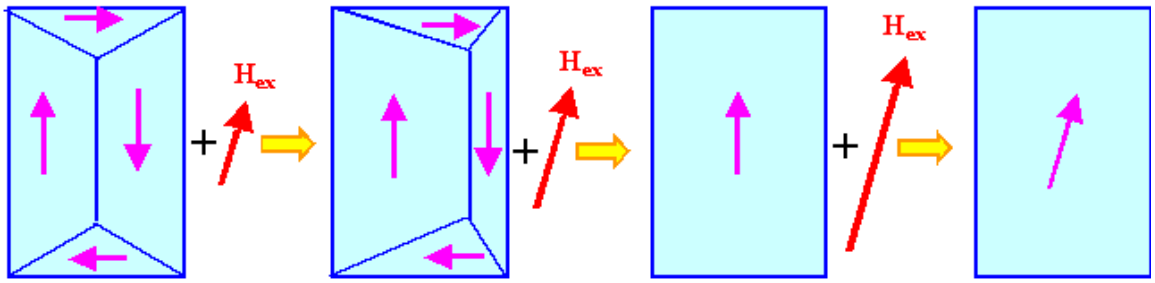

Figure 2.6: Movement of magnetic domains. Application of magnetic field rotates the magnetization of the individual domain into its own direction.

equations [22] describe this unique interest relating the microscopic electric and magnetic fields in the superconductors. Let the superconducting charge carriers have a density n_s and m and e be the electron's mass and charge respectively, then we can write the London equations:

$$\mathbf{A} = -\frac{m}{n_s e^2}\mathbf{J} \tag{2.10}$$

$$\mathbf{B} = -c\nabla \times \frac{m}{n_s e^2}\mathbf{J} \tag{2.11}$$

Taking the curl of both sides of Eq. 2.11 , and using Maxwell's equation, we obtain

$$\nabla^2\mathbf{B} = \mathbf{B}/\lambda^2 \tag{2.12}$$

and by extension:

$$\nabla^2\mathbf{J} = \mathbf{J}/\lambda^2 \tag{2.13}$$

These equations predict that currents and magnetic fields in superconductors can exist only within a layer of thickness λ of the surface where λ, known as the London penetration depth, is given by $\lambda^2 = \frac{mc^2}{4\pi n_s e^2}$. This indicates that at an air-superconductor interface, a tangential magnetic field decays exponentially from the surface into a superconductor bulk.

2.2.2 Ginzburg - Landau (GL) Theory

Ginzburg and Landau [23] in 1950 proposed a phenomenological theory of superconductivity by introducing a complex pseudowave function ψ as an order parameter for the superconducting electrons such that their local density was given by

$$n_s = |\psi(x)|^2 \tag{2.14}$$

If ψ is assumed small and slowly varying in space, the free energy density g can be expanded in a series of the form

$$g = g_{n0} + \alpha|\psi|^2 + \frac{\beta}{2}|\psi|^4 + \frac{1}{2m^*}\left|\left(\frac{\hbar}{i}\nabla - \frac{e^*}{c}\mathbf{A}\right)\psi\right|^2 + \frac{H^2}{8\pi} \tag{2.15}$$

In the absence of fields and gradients, we have

$$g - g_{n0} = \alpha|\psi|^2 + \frac{1}{2}\beta|\psi|^4 \tag{2.16}$$

Minimizing Eq. 2.16 with respect to $|\psi|^2$ gives the condensation energy density

$$g - g_{n0} = -\alpha^2/2\beta = \frac{-H_c^2}{8\pi} \tag{2.17}$$

where H_c is the thermodynamical critical field

Minimizing the overall free energy (2.15) using a variational principle, they derived a differential equation for ψ with a corresponding equation for the supercurrent

$$J_s = \frac{e^*\hbar}{2im^*}(\psi^*\nabla\psi - \psi\nabla\psi^*) - \frac{e^{*2}}{m^*c}|\psi|^2 A \tag{2.18}$$

The GL theory introduces a characteristic length, the temperature dependent coherence length,

$$\xi(T) = \frac{\hbar}{|2m^*\alpha(T)|^{1/2}} \tag{2.19}$$

which characterizes the distance over which $\psi(\mathbf{r})$ can vary without undue energy increase. The ratio of the penetration and coherence length defines the GL parameter

$$\kappa = \frac{\lambda}{\xi} \tag{2.20}$$

Since λ and ξ diverge in the same way at T_c, this dimensionless ratio is approximately independent of temperature. For type I superconductor, $\kappa < 1/\sqrt{2}$. In this case, there is a positive surface energy associated with a domain wall between normal and superconducting material in the intermediate state. However, for type II superconductor, $\kappa > 1/\sqrt{2}$, i.e $\xi \ll \lambda$. This leads to a negative surface energy, so that the process of subdivision into domains should proceed until it is limited by the microscopic length ξ. Instead of a discontinuous breakdown of superconductivity in a first-order transition at H_c, there would be a continuous increase in flux penetration starting at a first critical field H_{c1} and reaching $B = H$ at a second critical field H_{c2}. Because of the partial flux penetration, the diamagnetic energy of excluding the field is reduced, so H_{c2} can be much greater than the thermodynamic critical field H_c.

2.3 Vortex Behavior in HTSC

When the first flux enters a type II superconductor, it is carried within an array of vortices sparsely distributed through the material. So long as the separation is large compared to λ, there will be negligible overlap or interaction of the vortices, so that each can be treated in isolation. We can approximate the free energy per unit length, ϵ_1 of a vortex line due to supercurrents thus:

$$\epsilon_1 \approx \left(\frac{\Phi_0}{4\pi\lambda}\right)^2 ln\kappa = \frac{H_c^2}{8\pi}\, 4\pi\xi^2\, ln\kappa \tag{2.21}$$

We can also calculate the interaction energy between two vortices since in the approximation of $\kappa > 1/\sqrt{2}$, the medium is linear and we may use superposition;

$$E_{12} = \frac{\Phi_0^2}{8\pi^2\lambda^2} K_0\left(\frac{r_{12}}{\lambda}\right) \tag{2.22}$$

This falls off as $r_{12}^{-1/2} e^{-\mathbf{r}_{12}/\lambda}$ at large distances and varies logarithmically at small distances. the interaction is *repulsive* for the usual case, in which the flux has the same sense in both vortices.

From the practical point of view, the most useful aspect of type II superconductivity has been the ability to make the superconducting solenoids which can supply steady high fields without dissipation of energy because of the resistanceless persistent current. As described earlier, the origin of this dissipation is the Lorentz force density $\mathbf{F} = \mathbf{J} \times \mathbf{B}$ which sets up an electric field in the direction of flow of the total current density J. In order to reduce or eliminate this dissipation in form of resistance, vortices have to be immobilized or *pinned*. A pinning force $\mathbf{F}_p$ of magnitude at least equal to $\mathbf{F}$ is necessary. It is this pinning which allows the system to sustain the Lorentz force between the flux and the current without flux motion and dissipation. When $|\mathbf{F}| < F_p$ the vortices will be at rest; whereas they will move if $|\mathbf{F}| > F_p$. The precise value of F corresponding to the volume pinning force F_p is specially significant. When the applied force density is equal to F_p the corresponding current density is defined as the critical current density, J_c. We now have

$$F_p = J_c B \tag{2.23}$$

or

$$J_c \equiv F_p/B \tag{2.24}$$

This is the conceptual definition of J_c. In this work, we will use the modified Bean critical state model to estimate the J_c.

2.4 Pinning Mechanisms in HTSC

As mentioned earlier, good pinning properties, i.e. high vortex pinning forces, are very important in HTSC in order to obtain high J_c and allow usage in electronic and power applications. In this section, I will briefly review the Larkin-Ovchinnikov theory of collective pinning [24] which desribes pinning by very small-sized defects and the theory of strong pinning by Ovchinnikov and Ivlev [25]. The latter theory was modified/extended to describe the field and thickness dependencies of J_c for very thin films by van der Beek *et al* [26]. This modification is what is extensively used to explain some of the results obtained for the thin YBCO films deposited on RABiTs substrates used in this work. Aside from these two, there are other pinning theories for pinning centers with different sizes, shapes, and distributions.

2.4.1 Larkin-Ovchinnikov Theory of Collective Pinning

In 1979, A.I. Larkin and Yu V. Ovchinnikov [24] proposed this theory to explain pinning by *random* and weak pinning sites in conventional (low T_c). The main observation is that if the vortices were perfectly *periodic* and *rigid*, they would not be effectively pinned by any *random* collection of pinning sites. The reason is that, for any position of the vortex relative to the material, an equal number of random pinning sites would exert forces f adding to the Lorentz force as opposing it, summing to zero net force. Once we allow for the elasticity of the vortex, however, the paths of individual flux lines can deviate from the ideal periodic arrangement of the Abrikosov lattice to take advantage of the opportunity to lower their energy by passing through favorable pinning sites, but at the expense of increasing the elastic energy of the vortex by deforming it.

The key idea is to describe the distortion of the vortex line in terms of correlation volumes, within which the vortex line is reasonably undistorted, but between which there are pinning-motivated shear and tilt distortions on a relevant scale. Thus, as illustrated in Fig. 2.7, the macroscopic sample volume is considered to be subdivided into correlation volumes V_c with length $\sim L_c$ along the field direction and transverse dimensions $\sim R_c$.

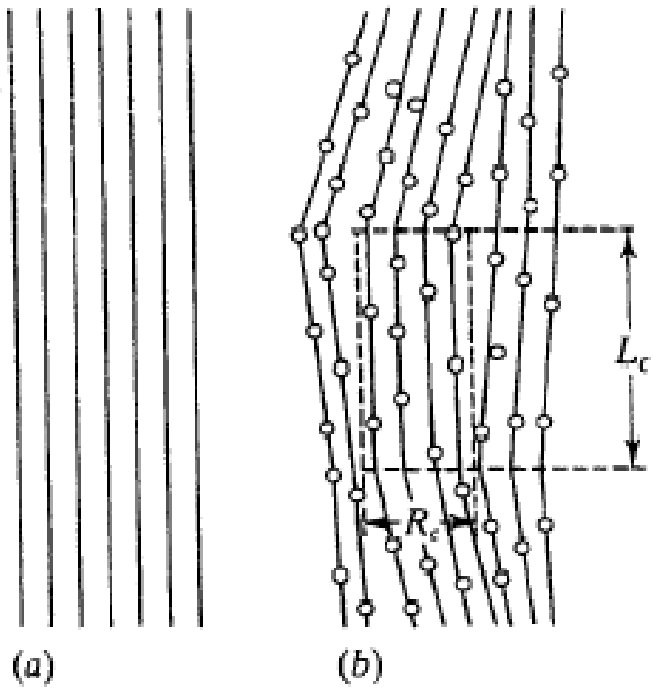

Figure 2.7: The coherence volume concept of the Larkin-Ovchinnikov theory. (a) With no pinning, the vortex line is periodic and exactly parallel to the magnetic field. (b) With random attractive pinning sites, the local direction of the vortex line is modulated slightly within each coherence volume (defined by R_c and L_c) so as to combine optimally the energy reduction from the pins with energy increase from distortion of the vortex line. (Figure from Tinkham.)

It is customary to describe the resulting increase in elastic free energy per unit volume as

$$\frac{1}{2}\left[C_{66}s_s^2 + C_{44}s_t^2\right], \tag{2.25}$$

where C_{66} and C_{44} are the elastic moduli of the vortex for shear and tilt, respectively. They can be estimated from inferences from the GL theory.

To find the corresponding pinning energy, we use the argument that the sum of N pinning forces in the correlation volume V_c, adding randomly, will be of the order of $N^{1/2}f$, where $N = nV_c$. Because this force acts only through a distance $\sim \xi$ before changing randomly, the amplitude of the associated potential energy will be $\sim \xi f N^{1/2}$, or $\sim \xi f n^{1/2}/V_c^{1/2}$ per

unit volume. If we subtract this energy gained by accomodating the pinning sites from the (positive) elastic distortion energy, we obtain the net free-energy change per unit volume from the presence of the pinning sites:

$$\delta F = \frac{1}{2} C_{66} \left(\frac{\xi}{R_c} \right)^2 + \frac{1}{2} C_{44} \left(\frac{\xi}{L_c} \right)^2 - f\xi \frac{n^{1/2}}{V_c^{1/2}} \tag{2.26}$$

Minimizing the above equation with respect to R_c and L_c gives

$$L_c = \frac{2C_{44}C_{66}\xi^2}{nf^2} \qquad R_c = \frac{2^{1/2}C_{44}^{1/2}C_{66}^{3/2}\xi^2}{nf^2} \qquad V_c = \frac{4C_{44}^2C_{66}^4\xi^6}{n^3f^6} \tag{2.27}$$

These results confirm the physical expectation that the vortex will be more distorted if there are more and/or stronger pinning sites, and if the elastic moduli are smaller.

Finally, the pinning force per unit volume determines the maximum sustainable Lorentz force density, so that the critical-current density J_c is given by

$$J_c B/c = \frac{n^2 f^4}{2C_{44}C_{66}^2\xi^3} \tag{2.28}$$

Insofar as these results hold, we see that a softer vortex (i.e., smaller elastic moduli) implies a larger pinning energy and larger critical current because the vortex can better conform to the pinning sites. In 2-D, such as in the case of a thin film or decoupled layers in a three-dimensional crystal, the collective pinning argument is modified because L_c is effectively set by d, the thickness of the film or layer. Accordingly, the critical current density is given by

$$J_c B/c = \frac{nf^2}{C_{66}\xi d} \tag{2.29}$$

Good agreement with the 2-D Larkin-Ovchinnikov model was found by Kes and Tsuei [27] in experiments on amorphous Nb_3Ge films

2.4.2 Strong Pinning by Sparse Large Point Pins

The theoretical development by Ovchinnikov and Ivlev [25] treats the case of large but relatively sparse pinning sites. In building this theory, they assumed that in order to obtain

J_c for sparse pins, one should not start from the statistical average of the pinning forces of the different defects, as in weak collective pinning of Larkin and Ovchinnikov [24] in the previous section, but rather evaluate the probability that a vortex line will be pinned at all. A nearby defect will be able to trap a vortex line if the gain in pinning energy $U_p^i \approx f_{p,max}^i \xi$ is sufficient to outweigh the elastic energy loss due to the vortex lattice deformation caused by displacing the vortex line onto the defect. The maximum allowed lateral displacement of the vortex u_0 determines the "trapping area" $\sim u_0^2$ within which a large defect is an effective pinning site. Van der Beek *et al* [26] updated the Ovchinnikov-Ivlev theory by offering an alternative explanation for the field and thickness dependence of the J_c measured in thin YBCO films. In the remaining of this section, I will give a summary of their theoretical development.

For a defect whose size along the field direction is given by D_z^i and D_i along the other directions, the pinning force can be estimated as:

$$f_{p,max}^i \approx \epsilon_0 \left(\frac{D_i^z}{4\xi}\right) ln\left(1+\frac{D_i^2}{2\xi^2}\right) \equiv \epsilon_0 \left(\frac{D_i^z}{4\xi}\right) F(T) \tag{2.30}$$

where $\epsilon_0 = \left(\phi_0/4\pi\lambda\right)^2 (4\pi/\mu_0)$ is the vortex line energy and $F(T)$ is a temperature dependent factor. From this and other considerations, the $J_c(H)$ can be approximated in three different regions thus:

$$J_c \approx 0.28\ n_i^{1/2} J_0 \frac{\left[D_i^z F(T)\right]^{3/2}}{2\epsilon}\ for H \ll H^* \tag{2.31}$$

$$J_c \approx 0.0866\ n_i J_0 \frac{\left[D_i^z F(T)\right]^{9/4}}{\epsilon^{5/4}\xi^{1/2}} \left(\frac{\Phi_0}{H}\right)^{5/8}\ for H \ll H_a \tag{2.32}$$

$$J_c \approx 0.375\ n_i J_0 D_i^z F(T) \frac{\Phi_0}{H}\ for H \gg H_a \tag{2.33}$$

Here, n_i is the defect density, J_0 is the depairing current density, $\epsilon = \sqrt{m_{ab}/m_c} \sim 1/5$ is the anisotropy parameter and Φ_0 is the flux quantum. Eq. 2.31 gives the J_c in the single-vortex

(low fields) limit where J_c is independent of the field. This is realised for fields lower than a characteristic value H^* which is given by:

$$H^* \equiv \pi \Phi_0 n_i (U_p/\epsilon_0) \quad for H \gg H_a \tag{2.34}$$

In Eq. 2.32 and Eq. 2.33, H_a is a crossover field at which the maximum allowed lateral vortex displacement u_0 becomes comparable to the vortex spacing a_0.

In a simplified development based on the work of Vinokur et al, [28], van der Beek [26] developed alternative expressions for the critical current density in the intermediate field regime with interacting vortices, obtaining

$$J_c = 0.087 \; n_i J_0 \frac{[D_i^z F(T)]^2}{\epsilon} \left(\frac{\Phi_0}{B}\right)^{1/2} for B \ll \widetilde{B}_a \tag{2.35}$$

where the characteristic field is given by

$$\widetilde{B}_a = \Phi_0 \left(\epsilon \frac{\epsilon_0}{U_p}\right)^2 \tag{2.36}$$

As a function of thickness d, the prediction is that $J_c \propto d$ for very thin films (thin-thin films), with

$$J_c = n_i \frac{D_i^z}{4\xi} F(T) \frac{U_p}{\Phi_0 \epsilon^2} d \tag{2.37}$$

For thicker films (thick-thin films), the J_c becomes independent of d, theoretically, above a crossover thickness d^*. This crossover from the thin-thin films to the thick-thin films occurs near the thickness

$$d^* = \left[\frac{\epsilon^2 \epsilon_0}{\pi n_i U_p}\right]^{1/2} \tag{2.38}$$

which is determined by consideration of the trapping area in either limit.

Furthermore, from this model, the density of defects/pinning sites n_i can be deduced.

2.5 The Modified Bean Critical State Model

The critical current density J_c will in general depend on both $\mathbf{r}$ and $\mathbf{H}$. This fact tends to complicate the analysis of the critical current condition substantially. Bean [29, 30] suggested to model J_c as a constant corresponding to regarding $J_c = dH/dx$ as constant in a bulk superconductor.

From electrodynamics, we know that a circulating current generates a magnetic dipole moment according to the equation

$$m = (1/2c) \int (\mathbf{r} \times \mathbf{J}(\mathbf{r}))\, dV, \tag{2.39}$$

where $\mathbf{J}$ is the current density at location $\mathbf{r}$. The hysteresis in magnetism curves of superconductors as depicted in Fig. 2.8 allows J_c to be determined with the help of the Bean model [29, 30]. This model is based on two simple assumptions, namely that the supercurrent density is given by a J_c and that any changes in the flux distribution are introduced at the sample surface. In essence, the model provides that $J_c(H,T)$ is proportional to $\Delta M = (M^- - M^+)$ where $M^-(M^+)$ is the magnetization at temperature T measured in decreasing (increasing) field history, respectively.

For a rectangular solid with field perpendicular to a face with sides $b > a$, the "sandpile" model [31] provides that

$$J_c = \frac{20\Delta M}{a\left(1 - \frac{a}{3b}\right)} \tag{2.40}$$

where in practical laboratory units, ΔM has units of Gauss, lengths are in cm and J has units of A·cm^{-2}.

The simple and very useful rule we glean from this is that the wider the magnetization loop is, the higher is J_c. Before computing the J_c value in RABiTS materials, the signal from the ferromagnetic substrate was subtracted out.

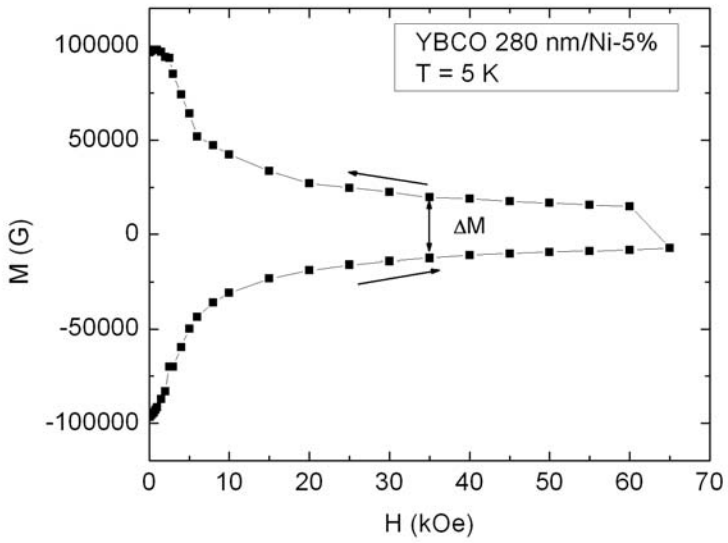

Figure 2.8: The hysteresis in the magnetization curve of a superconductor. A plot of $M(H)$ showing the hysteresis in the magnetization curve of a 280 nm thick YBCO film. (In this data, the signal from the ferromagnetic substrate has been substracted out.)

2.6 AC Loss

The three main sources of ac loss for the coated conductor geometry in this work are: (a) Hysteretic loss from the superconductor (b) Ferromagnetic (FM) hysteretic loss in the alloy substrate and (c) Eddy loss as a result of eddy currents generated in the substrate. The last source of ac loss is negligible in our case. The initial part of this work deals with measuring and understanding the second form of loss, i.e. from the alloy substrate. The main equation we used in calculating the FM loss is:

$$Loss_{FM} = \mu_0 \oint (MdH)\ (energy/mass) \tag{2.41}$$

This represents numerically integrating the $M(H)$ loop to obtain its area which is related to the energy dissipated every time the magnetization is taken around the loop. M here is the mass magnetization.

The ac loss from the superconductor arises from the time varying magnetic field. This form of loss is also hysteretic in nature and can be measured experimentally by using Eq. 2.41. In his famous work on calculating the hysteretic losses in hard superconductors, Norris [18] derived two expressions for the ac loss in conductors with elliptic and thin strip geometries as a function of the peak current ratio, $F = I_p/I_c$, which can be written respectively as

$$Loss_{sc} = \frac{\mu_o I_c^2}{\pi}[(1-F)ln(1-F) + F - F^2/2] \ (energy/length) \tag{2.42}$$

and

$$Loss_{sc} = \frac{\mu_o I_c^2}{\pi}[(1-F)ln(1-F) + (1+F)ln(1+F) - F^2] \ (energy/length) \tag{2.43}$$

Here the terms thin strip and elliptical geometry refer to the relative ratio of the superconductor width to its thickness. In the low current limit, hysteresis losses in the thin strip model vary as $(I_p/I_c)^4$, while the elliptic model predicts hysteretic loss proportional to $(I_p/I_c)^3$. Thus, the total loss for this geometry can be written as $\text{Loss}_{tot} = \text{Loss}_{sc} + \text{Loss}_{FM}$ where Loss_{FM} is calculated by using Eq. 2.41. For dimensional consistencies, values obtained from Eq. 2.41 are multiplied by a "length density" i.e. FM mass/length in order to be able to do the summation. This estimate of the total loss agrees well with the experimentally measured values from RABiTS coated conductors with Ni-5at.%W as substrates [32].

Chapter 3

Experimental Methods

The first section in this chapter will describe the preparation of materials while the second section will briefly discuss the characterizing techniques of X-ray diffraction (XRD) and transmission electron microscopy (TEM). In the third section, the techniques used while performing the experiments will be discussed and the last section will focus on the magnetometry details.

Experimental studies were conducted to determine (1) magnetic properties of "bare" metallic substrate materials and (2) low-loss current conduction in SC layers

The different samples used in this work were made by various methods. $Ni_{1-x}W_x$ materials with nominal compositions x = 0, 3, 5, 6, and 9 were used in the first part of the project. These alloys were formed by either vacuum melting or by powder metallurgy methods. In the second part, the YBCO films of various thicknesses were prepared on buffered Ni-W substrates using an $ex - situ$ process.

3.1 Sample Creation

The magnetic and ferromagnetic properties of a series of biaxially textured Ni-W alloys were studied in the first part of this project. These materials are important as substrates for RABiTS type coated conductors. Different steps were involved in the two types of methods used in making these alloys. In the final step, the recrystallization by annealing

was done at temperatures in the range T_{ann} = 950 - 1150 ^{o}C for the vacuum cast (VC) materials and 1300 ^{o}C for the powder metallurgy (PM) alloys. The maximum temperature is limited by the need to avoid secondary recrystallization, which destroys the desired biaxial texturing. All the Ni-W alloys used have thicknesses of 50 - 75 μm with typical dimensions of 3 - 4 mm by 3.5 - 4 mm and they were provided by our collaborators at the Oak Ridge National Laboratory (ORNL), Oxford Instruments Superconducting Technology and American Superconductor Corporation (AMSC).

Efforts to improve the synthesis methods of growing epitaxial YBCO superconducting films have led to the physical vapor deposition (PVD) BaF_2 *ex-situ* process. This method is well suited for YBCO coatings on both RABiTS and IBAD templates. The main distinct feature in this method is the reaction/phase formation after deposition (post-annealing) of the films as opposed to an *in-situ* process where the annealing is done at the same time as the deposition.

3.1.1 Vacuum Casting/Melting

Once almost exclusive to the aerospace industry, vacuum precision casting now has found new markets as engineers strive to improve the quality and performance of metals and alloys in a counteless number of applications. The superconductivity field is one of these.

Certain alloys containing chromium, nickel, cobalt, etc have a strong affinity for oxygen. If these alloys are melted in air, the severe oxidation reaction that occurs seriously impairs the final properties of the cast product. This is the main reason why these high performing castings are processed in the molten state under vacuum, which ensures that there is minimal oxidation during melting. Electromagnetic induction is used as the energy source for melting the metal. The necessary vacuum level is easily achieved in modern vacuum melting equipment. From the primary alloy production through investment casting and to the final heat treatment, all thermal processing is carried out under vacuum. Fig. 3.1 shows the vacuum melting flow diagram.

The three main steps involved in the VC process are casting, rolling and recrystallization. Starting with very pure nickel and the desired amount of tungsten, this mixture is introduced

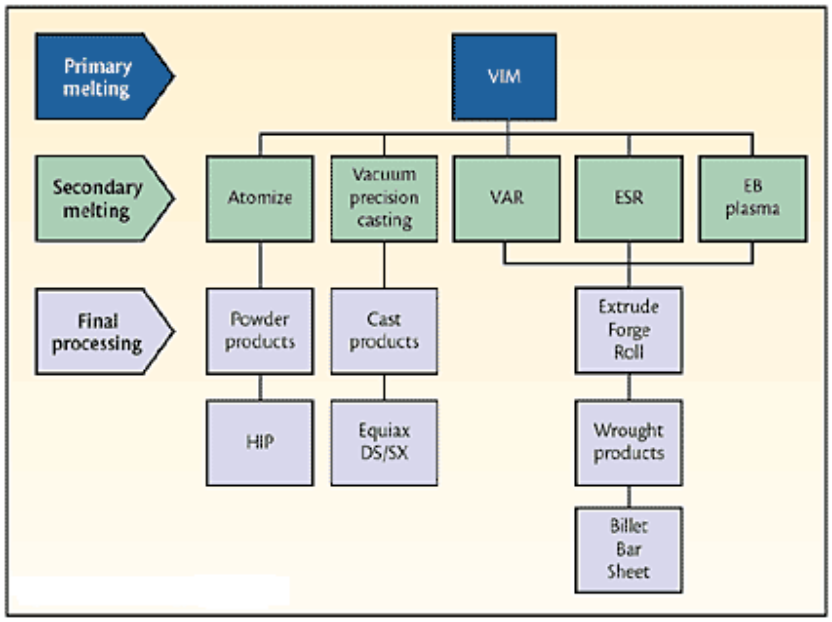

Figure 3.1: Vacuum melting flow diagram. All thermal processing is carried out under vacuum. DS/SX = directionally solidified/single crystal; EB = electron beam; ESR = electroslag remelting; HIP = hot isostatic pressing; VAR = vacuum arc remelting; VIM = vacuum induction melting.

into a mold while it is liquid, allowed to solidify in the shape inside the mold, and then removed. The rolling stage is when the solidified material is cold rolled to form fine sheet and to produce the desired cube texture. The recrystallization process is when the alloy is texture annealed in order to toughen and reduce brittleness. This is done at a temperature of 950 - 1150 ^{o}C.

In past years, all vacuum melting furnaces were manually operated and it was not uncommon to have significant variances in product quality dependent on the operators involved. Today, computer-based control systems have fully automated the procedures. All furnace operations can then be performed automatically, thus maintaining consistency between casts.

3.1.2 Powder Metallurgy

Powder metallurgy involves blending of powders of metals or metal oxides together using an organic binder in this case, some form of hydrocarbon wax. Direct production of Ni-W alloy strip up to about 8 km in length and 0.05 mm in thickness has been achieved.

A high purity carbonyl nickel powder with properties suitable for roll compaction mixed with the desired amount of an equally high purity tungsten powder is obtained commercially. These powders are then cold compressed into a thin strip using two horizontally opposed rolls. A mechanical bond between the powder particles imparts sufficient strength to the powder compact so it can be guided from beneath the compaction rolls and fed onto a conveyor belt and into a sintering surface. The sintered strip is subjected to additional thermal and cold rolling steps to achieve full density and chemical homogeneity. The rolling and sintering processes are done at a temperature of about 1100 ^{o}C while the homogenization is done for 48 hours at 1400 ^{o}C. Fig. 3.2 shows the roll compaction process.

The final stage in the production is the texture annealing (recrystallization). All annealing is performed in hydrogen-containing atmospheres. For PM alloys, this annealing can be done at a higher temperature (1300 ^{o}C) than the VC alloys. This is one of the main differences in the two processes. For the PM alloys, annealing at a higher temperature

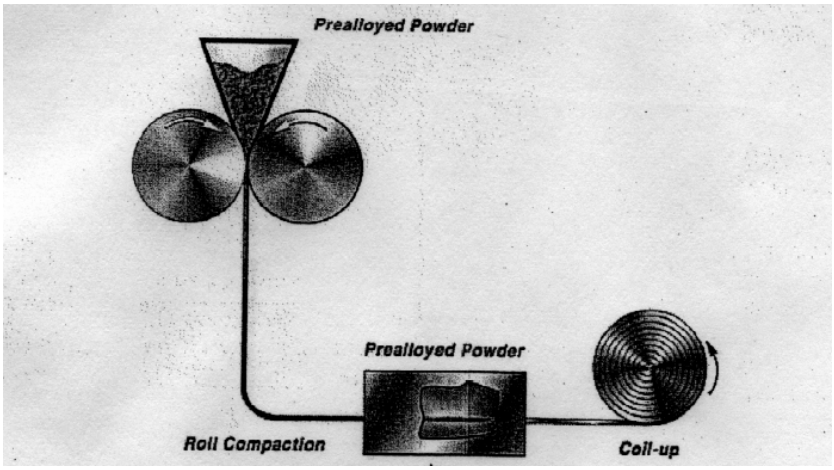

Figure 3.2: The roll compaction process of the PM method. The process runs continuously as powder blends are consumed and replaced with fresh powder, hence, very long coil lengths are possible.

should qualitatively lead to a lower density of dislocations and related structural defects which ultimately leads to them being less lossy than their VC counterparts [15].

Other features of PM alloys are very low impurity level (although TEM images have shown presence of carbides) and excellent consistency over strip length, corresponding to the uniformity of the initial powder blend.

3.1.3 PVD BaF_2 *ex-situ* Process

As suggested by the layered geometry in YBCO, the critical currents I_c can be enhanced by either increasing the YBCO layer thickness d, or alternatively, for a suitably large value of d, focus on process optimization in order to increase the critical current density J_c. The PVD (Physical Vapor Deposition) BaF_2 *ex-situ* process for YBCO epitaxial film growth is one of the better ways of growing these films. It has been under development for CC applications at least since 1998 [33]. Recent efforts have focused on defining new processing parameters to enable faster conversion of the precursor into YBCO. The faster processes are suitable for large-scale applications.

In this process, PVD BaF_2 precursors are annealed to form epitaxial YBCO films of various thicknesses d on buffered Ni-W substrates. The post-deposition annealing (*ex-situ*) is usually conducted at atmospheric pressure under a flowing gas mixture of oxygen, water vapour and a carrier gas of nitrogen or argon.

For the precursors of the desired $YBa_2Cu_3O_{7-\delta}$ phase, barium exists in a molecular state as BaF_2. The epitaxial nucleation and growth of YBCO during the processing anneal is directly related to the decomposition of BaF_2, i.e., according to the effective reaction [34]

$$\frac{1}{2}Y_2O_3 + 2BaF_2 + 2CuO + \frac{1}{2}Cu_2O + 2H_2O \rightarrow YBa_2Cu_3O_{6.0} + 4HF \qquad (3.1)$$

To deposit the precursors, films of various thicknesses were deposited by simultaneous electron-beam evaporation from sources of Y, BaF_2 and Cu sources. Quartz crystal monitors (QCM) were used to measure and control the three individual evaporation rates

while the compositions of the precursor films were determined subsequently by Rutherford backscattering spectroscopy (RBS).

During deposition, the substrates were slightly heated to $\sim$ 100 ^{o}C. Small amounts of O_2 were introduced into the vacuum chamber to partially oxidize the deposit and minimize reduction of substrate CeO_2 buffer layers.

Post-deposition anneals were carried out in an induction vacuum furnace whose configuration is schematically shown in Fig. 3.3. This furnace is equipped to operate with flowing gas mixtures at atmospheric pressure. Thickness values d were inferred from the combined QCM readings, calibrated against profilometry and RBS measurements after conversion. The films have thicknesses from 28 to 1500 nm.

RABiTS substrates used were provided by the American Superconductor Corporation (AMSC). They feature a 75 μm thick Ni-5%W deformation-textured metal template with average grain size of $\sim$ 25 μm, and epitaxial Y_2O_3, YSZ and CeO_2 buffer layers.

3.2 Sample Characterization

X-ray diffraction is a powerful tool for finding the crystallographic orientation of created samples. The main idea involved is the *Bragg condition* of constructive interference, given by

$$n\lambda = 2asin\theta \tag{3.2}$$

Here λ is the wavelength of the X-rays, θ is the angle that the X-rays make with the reflecting plane, n is the order of the reflection and a is the separation of the planes, as illustrated in Fig. 3.4.

XRD performed on some of the Ni-W alloys showed that thermomechanical processing produced nearly complete $\{100\}\langle100\rangle$ cube texturing as desired for applications. Also, for the YBCO films, this technique was used for their structure characterization and morphology inspection. A Philips model XRG3100 X-ray diffractometer with Cu Kα radiation was used to record powder $\theta - 2\theta$ diffraction patterns.

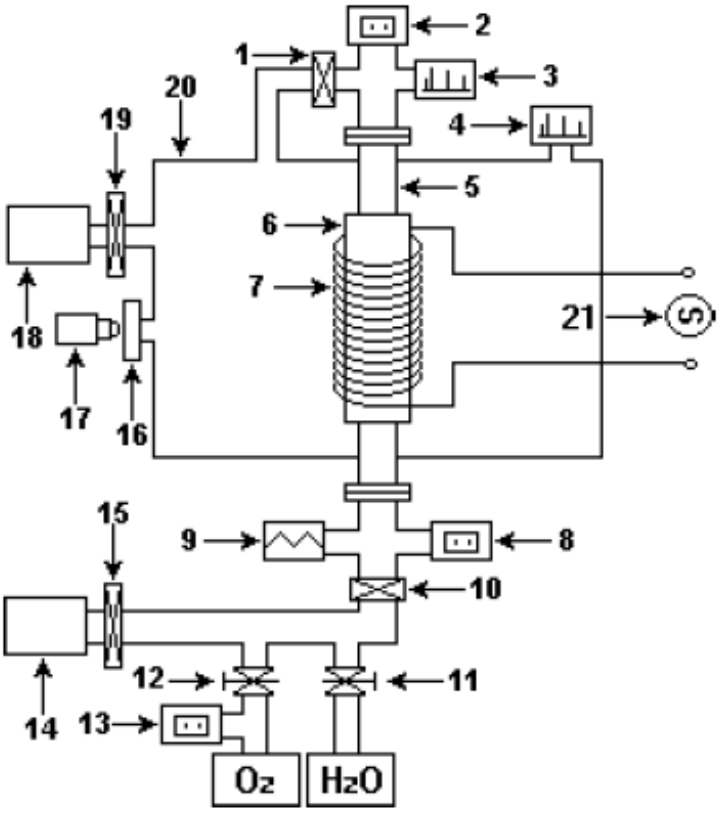

Figure 3.3: Schematic configuration of the post-annealing induction vacuum furnace system. 1, 10, 15 - valves; 2, 8 - convectron vacuum gauges; 3, 4 - residual gas analyser (RGA) detectors; 5 - quartz tube with sample inside; 6 - susceptor; 7 - induction coil; 9 - ionization vacuum gauge; 11, 12 - variable leak valves; 13 - capacitancemanometer; 14 - roughing pump; 16 - view port; 17 - pyrometer; 18 - cryopump; 19 - gate valve; 20 - UHV chamber; 21 - RF generator. (Figure from [34].)

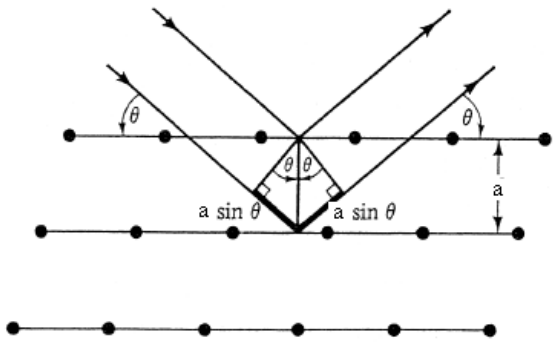

Figure 3.4: A schematic of the Bragg condition in XRD. (Figure from Ashcroft and Mermin.)

Transmission electron microscopy is an imaging technique whereby a beam of electrons is focused onto a specimen causing an enlarged version to appear on a fluorescent screen or layer of photographic film, or can be detected by a CCD camera (a special detector silicon called a charge-coupled device (CCD)). This microscope works on similar principles to those of a light microscope. Resolution can be quite high with a TEM due to the much smaller wavelength of energetic electrons. This is why this device is extremely useful for studies of systems at the nanometer scale.

Transmission electron micrographs of a few of the thin superconducting films were obtained. Planar views using a High-Resolution TEM (Phillips CM200UT with Ge EDS) of the films were taken, primarily to determine the sizes and compositions of the defects in the YBCO. More of this is discussed in the chapter on results.

3.3 Experimental Techniques

3.3.1 Magnetic Studies of Ni-W Alloys

For the magnetic studies of the $Ni_{1-x}W_x$ materials with nominal compositions x = 0, 3, 5, 6, and 9 at.%, a sample of tape, with typical dimensions of 3 - 4 mm × 3.5 - 4 mm and thickness of 50 - 75 μm, was mounted in a SQUID - based magnetometer, either a Quantum Design model MPMS-7 or a model XL with ac capabilities. The tape was vertical with the magnetic field H applied parallel to the sample's surface, in order to minimize demagnetizing effects. Temperatures ranged from 5 to 375 K in fields up to 15 kOe. We measured both the isothermal mass magnetization $M(H)$ at different fixed temperatures and $M(T)$ in fixed field. For the FM loss studies, we measured one complete loop of the quasi-static dc magnetization $M(H)$, starting from field $+H_{max}$ and sweeping to field H_{max}, then back to field $+H_{max}$. This process was repeated at progressively higher field amplitudes H_{max} in the range 5 - 400 Oe. For example, in a 100 Oe cycle, (H_{max} = 100 Oe) the sample was first "exercised" by applying a magnetic field H = +100, -100, +100 and -100 Oe, to simulate several cycles of ac field in an application and to establish the steady state ferromagnetic response. Then the loop $M(H)$ (in units of G cm^3/ g) was measured,

sweeping the field in small increments from +100 to -100 Oe and back to +100 Oe. In any conductor configuration, the field excursion H_{max} will increase with the amplitude of the ac current, with a geometry-dependent proportionality [32]. Measurements of FM loss were done at $T = 50$ and 77 K which are proposed operating temperatures for the coated conductors. In some cases, the ac magnetization was measured, in order to see if the FM loss/cycle depended on frequency. Frequencies ranged from 2.5 to 600 Hz, with ac field amplitudes h_{ac} up to 6.8 Oe peak. In one case, a bias dc field was applied parallel to the ac field to assess its influence. For the deformation studies, we used a common bending strain of 0.4% for all the samples deformed. Using the formula

$$bending\ strain = \frac{thickness\ of\ sample}{diameter\ of\ mandrel} \quad , \tag{3.3}$$

an appropriate mandrel was used to deform each of the samples. A sample was wrapped around the mandrel and then flattened to complete a half-cycle of deformation; when reverse wrapped and again flattened, the tape completed one complete deformation cycle. The objective of this bending study was to simulate the work hardening that might be encountered during handling or fabrication of electrical equipment, e.g., during winding operations. In addition, we determined the increase in loss associated with cutting the Ni-W alloy substrate, as might be encountered in slitting operations following final fabrication of a coated conductor. Finally, the effect of temperature cycling was investigated for one sample, by dipping it in liquid nitrogen, warming it to room temperature, and then immersing it again. This thermal cycle was repeated eight times, after which the FM loss was remeasured in a 400 Oe cycle at 77 K.

3.3.2 Critical Currents of YBCO Thin Films

For the superconducting thin films, their J_c values were magnetically determined by applying the modified critical state model to the magnetic hysteresis via the relation given by Eq. 2.40. All measurements were done in a SQUID-based magnetometer, a Quantum Design model MPMS-7 with a maximum field of 7 T. Both isothermal magnetization loops

$M(H;T)$ and remanent magnetization $M_{rem}(T)$ in $H = 0$ were measured, with H applied perpendicular to the film plane i.e. $H \parallel$ c - axis. For the isothermal magnetization measurements, fields in the range 0 - 6.5 T were applied at different fixed temperatures (5 - 95 K) and the moment generated by the induced flowing current in the film was measured. For the remanent magnetization measurement, a large field (~ 0.5 T) was first applied to set up currents in the film. This field was then gradually taken off, thereby inducing currents in the opposite direction. The magnet in the SQUID was reset to ensure that H was truly zero before measurements were taken, and to provide a very quiet measurement environment. Signals of the reversible background magnetization from the ferromagnetic substrate were subtracted out before computing the J_c. These two ways of determining the J_c at self - field are complementary and yield very similar results.

In order to determine the superconducting transition temperature T_c for the films, temperature-dependent measurements of $M(T)$ were made in an applied field of 10 Oe (after cooling to 5 K in zero applied field). The resulting values for the onset temperature T_c range from 88 to 91 K for the films.

3.4 The SQUID Magnetometer

All the magnetic measurements in this work were performed using a SQUID (Superconducting QUantum Interference Device)- based magnetometer. This device is highly sensitive to magnetic field and moment. It can measure changes in magnetic flux on the order of one hundrendth of a flux quantum. Magnetic flux in a superconductor is quantized in units (SI units)

$$\phi_o = \frac{h}{2e} \cong 2.0678 \times 10^{-15} \quad T \cdot m^2 \tag{3.4}$$

Our SQUID magnetometers, a commercial system by Quantum Design, can measure smallest magnetization down to $\sim 10^{-8}$ emu and up to 300 emu. The range of field is 0.05 G to 70 kG with a uniformity of 0.01% over 4 cm for both the MPMS-7 and XL

models. The XL model has an added capability to measure ac field up to 6.8 Oe with a frequency range of 0.001 to 1000 Hz. The temperature range is 1.9 to 400 K with an accuracy of 0.01 K. A SQUID - based magnetometer works on the principle of Josephson junctions [35]. It consists of a sensor, which is comprised of a superconducting ring interrupted by one or two thin insulating layers (weak links) to form parallel Josephson junctions. Fig. 3.5 is a schematic representation of a SQUID magnetometer.

If a constant biasing current is maintained in the SQUID device, the measured voltage oscillates with the changes in phase at the two junctions, which depends upon the change in the magnetic flux. This measured voltage, when properly calibrated using a sample of known magnetic moment, can be used to provide accurate values for the magnetization of the

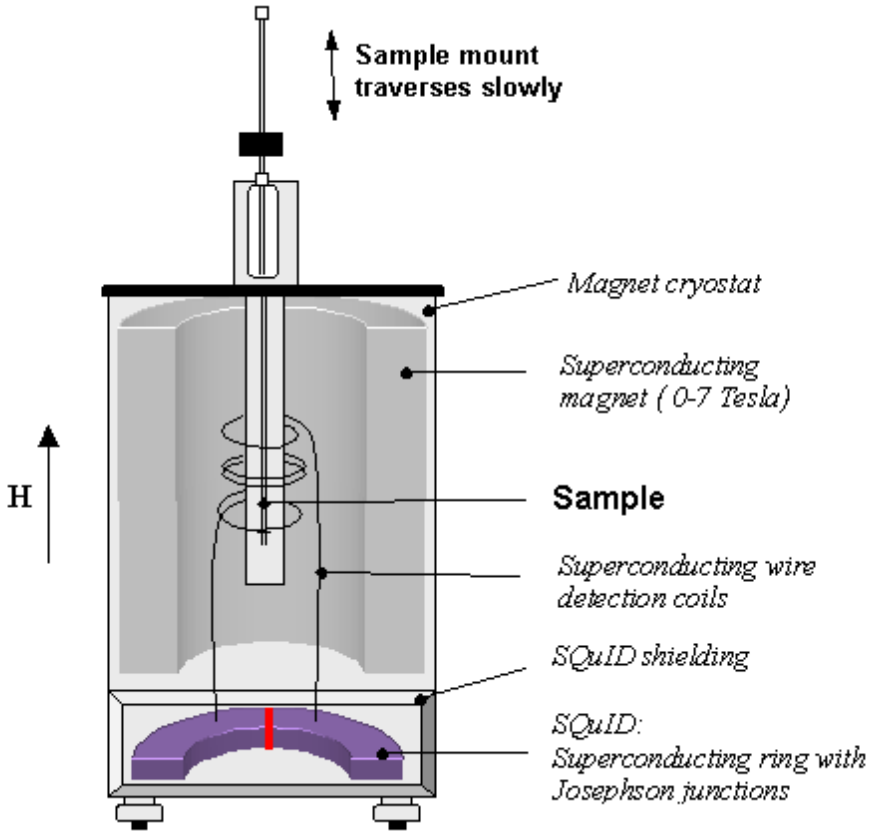

Figure 3.5: Schematic diagram of a SQuID magnetometer

sample. The sample, mounted on one end of the sample rod within a plastic straw, is moved slowly through a set of detection coils coupled to the SQUID sensor via superconducting wires. This system of detection coils and superconducting wires forms a flux transformer that helps solve the problems of external field influence. It is a continuous superconducting wire that is wound as an inductor at one end and as a second-derivative coil in the sample space, illustrated in Fig. 3.6.

There are three coil sections; the bottom and top have a single winding in the clockwise direction while the middle section has two windings in the counter-clockwise direction. A well balanced second derivative coil would be insensitive to external field because the number

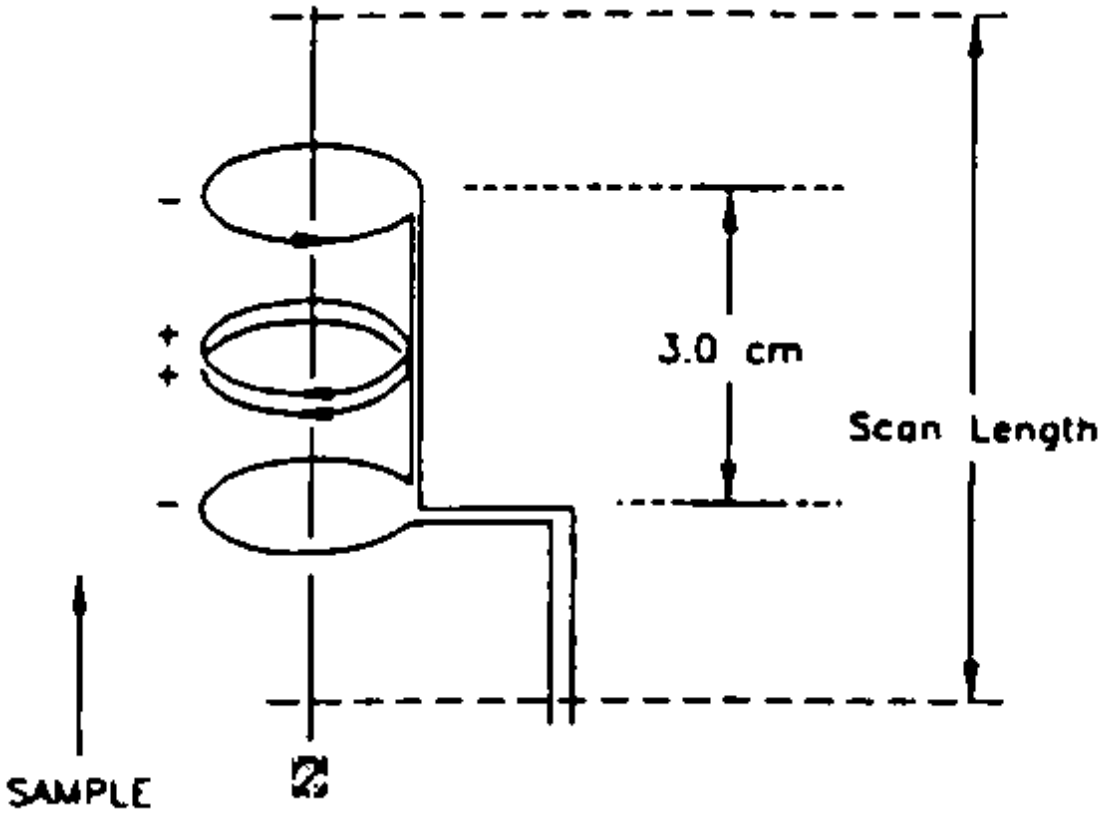

Figure 3.6: A flux transformer with a second-derivative coil geometry in the sample space.

of clockwise and counter clockwise turns is balanced. It is also insensitive to a uniformly varying field. The output voltage as a function of position for a magnetic moment being moved through the second-derivative coil is shown in Fig. 3.7. This scan pattern can then be fit to what would be expected behavior from a perfect dipole moving through the array.

To confirm proper operation of the moment and applied field scales of the magnetometer, a calibration with standard samples can be performed. More on this calibration technique is discussed in one of the appendices in K.D. Sorge dissertation.

The applied magnetic field is produced by a superconducting magnet, one made of niobium-titanium. Nb-Ti has a critical temperature of about 9.8 K, hence to keep it superconducting and also for cooling the sample space, a constant supply of liquid helium is needed when the magnetometer is being used. This liquid helium is stored in the surrounding dewar.

In addition to measuring magnetization as a function of applied field/temperature, the XL model SQUID magnetometer also has the capabilities of doing ac measurements. Here, the quantity of interest is the ac susceptibility $\chi = \frac{dM}{dH}$ which is the amplitude of a periodic magnetic moment induced by a small oscillating magnetic field . The applied field is varied by a programmable waveform synthesizer.

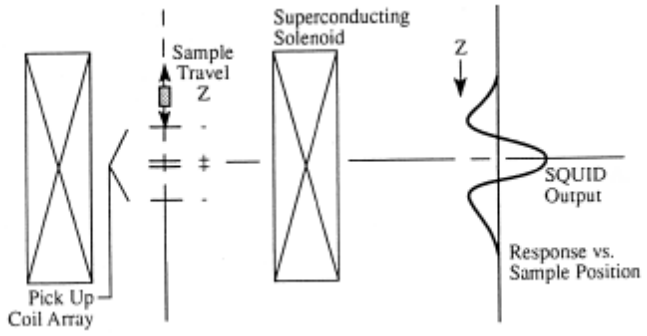

Figure 3.7: The output voltage of the magnetometer as a function of sample position.

Chapter 4

Experimental Results

This chapter is broadly divided into two sections. The first section deals with results obtained from studying the magnetic and ferromagnetic properties of Ni-W alloys. Here, both the intrinsic and extrinsic properties would be reported. Many aspects of this study were reported in a paper published in the journal Physica C in 2004 titled "Magnetism and ferromagnetic loss in Ni-W textured substrates for coated conductors". The citation is: A. O. Ijaduola, J. R. Thompson, A. Goyal, C. L. H. Thieme, and K. Marken, Physica C **403**, 163 (2004).

My primary contributions to this paper include (1) designing and performing all the experiments, (2) analysis and interpretation of the data, (3) gathering all the resources and references needed in writing the paper, and (4) most of the writing.

The second section deals with the critical current density J_c measured in the YBCO films deposited on "RABiTS" substrates of Ni-5at.%W.

4.1 Magnetic Properties of Ni-W alloys

4.1.1 Saturation Magnetization

For an overall perspective , Fig. 4.1 shows the mass magnetization M plotted versus applied field H for all compositions studied. The measurements were done at $T = 5$ K in fields H up to 10 kOe, in order to obtain the saturation magnetization M_{sat}. The values of M_{sat} steadily

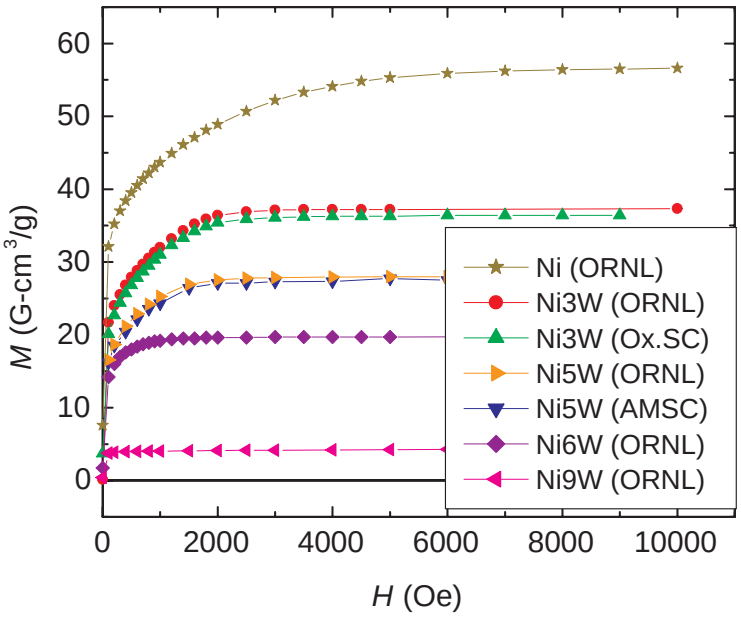

Figure 4.1: Magnetization M of $Ni_{1-x}W_x$ alloys versus applied magnetic field H. Annotations in figure show W-content x in atomic percent, e.g., Ni3W = 3at.%W. Measurements were done at $T = 5$ K.

decrease with the addition of tungsten which shows that the more the content of W in these alloys, the less ferromagnetic they become. In order to see this feature clearly, we make a plot of M_{sat} versus W-content x in Fig. 4.2. The figure reveals a variation with x that is very nearly linear, similar to that observed in Ni-Cr alloys.[36, 14] A linear extrapolation to $M_{sat} = 0$ intersects at a critical W-concentration $x_c = 9.55 \pm 0.40$ at.%. Long ago, the magnetic properties of this alloy system were studied by Marian [37]. The results were subsequently reported in Bozorth's book [38] and still later in a data compilation[39]. The data of Marian are included in Fig. 4.2.

4.1.2 Curie Temperature

We determined the Curie temperature T_c for several alloys from temperature-dependent measurements of the magnetization $M(T)$. The analysis was based on the relation that the

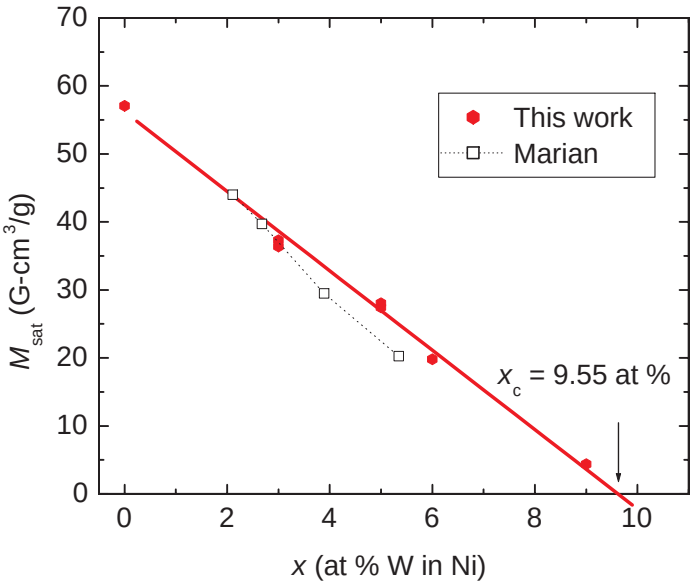

Figure 4.2: Variation of saturation magnetization of $Ni_{1-x}W_x$ alloys with W-content x. Included are values obtained here and those reported by Marian [37]. The line is a linear dependence fitted to the present data and extrapolated to the critical concentration x_c.

spontaneous magnetization varies with temperature as $M \propto (T_c - T)^\beta$ with $\beta \approx 1/3$ for a 3D Heisenberg magnet.[40]

In approximating the spontaneous magnetization by the bulk signal, we ignore all data very close to T_c due to the influence of the applied field. The process is illustrated in Fig. 4.3, which shows M^3 plotted against T for two alloys, Ni-5at.%W and Ni-6at.%W. The substantial region of linearity shows that the "critical point" relation given above describes the system rather well. The Curie temperature was obtained by a linear extrapolation to $M^3 = 0$. The resulting values of T_c are presented in Fig. 4.4 as a function of W-concentration x. Again, the values of Marian [37] are included for comparison.

As with the saturation magnetization M_{sat}, we observe a nearly linear decrease with x; a linear extrapolation to $T_c = 0$ gives a value for the critical concentration $x_c = 9.75 \pm 0.40$ at.%, which is consistent within experimental error with the result from M_{sat}.

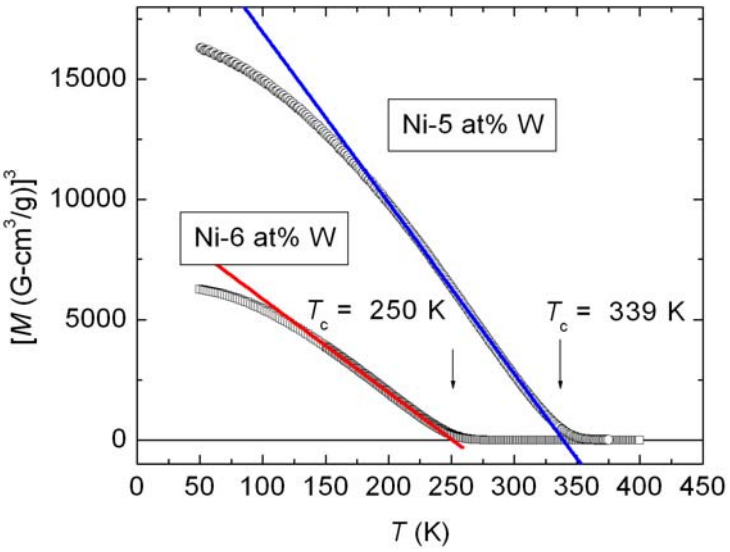

Figure 4.3: M^3 versus temperature T for Ni-5at.%W and Ni-6at.%W. Straight lines show the extrapolation to $M = 0$ used to define Curie temperature.

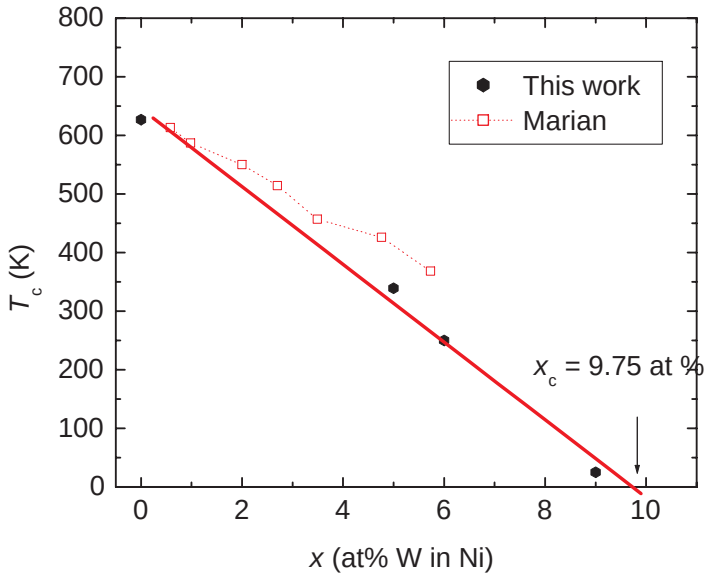

Figure 4.4: Dependence of Curie temperature of $Ni_{1-x}W_x$ alloys with W-content x. Shown are present results and those of Marian [37]. The straight line extrapolates to the critical concentration x_c.

This implies, perhaps more fundamentally, that M_{sat} and T_c are proportional in these Ni-W (and also the Ni-Cr) alloys. Table 4.1 lists these two parameters for the present materials.

4.1.3 AC Loss

Next, we consider the hysteretic energy loss in these ferromagnetic Ni based materials. To illustrate some essential features, we show in Fig. 4.5 several plots of magnetization M vs H for a rather lossy sample of electroplated Ni, at $T = 120$ K. Included are curves for cycles with $H_{max} = 100$, 200, 400 and 800 Oe. Qualitatively, it is clear that the area inside the loop increases as the field excursion increases, and then saturates when the material becomes reversible in sufficiently large fields. This is the general behavior for the biaxially textured substrate materials also, but their loops are much more narrow and the changing area is less visible. To obtain the hysteretic energy loss/cycle W, we numerically integrate each $M(H)$ loop to obtain its area (in units of erg/gram-cycle). Many of these results are collected in Fig. 4.6, a plot of loss W versus field excursion H_{max}. The general response of these soft ferromagnetic materials (coercive fields of a few Oe) is similar, with a roughly linear variation at low field amplitudes H_{max}, followed by saturation at higher field amplitudes. As the temperature decreases, the loss W increases as might be expected, but only slightly between 77 and 50 K (which are temperatures of application as coated conductor substrates).

Table 4.1: Magnetic properties of Ni-W alloys.

Material	M_{sat} $(G - cm^3/g)$	T_c (K)
Nickel	57.06	627
Ni-3at.%W	36.4 - 37.3	> 420
Ni-5at.%W	27.4 - 28.0	339
Ni-6at.%W	19.8	250
Ni-9at.%W	4.36	25

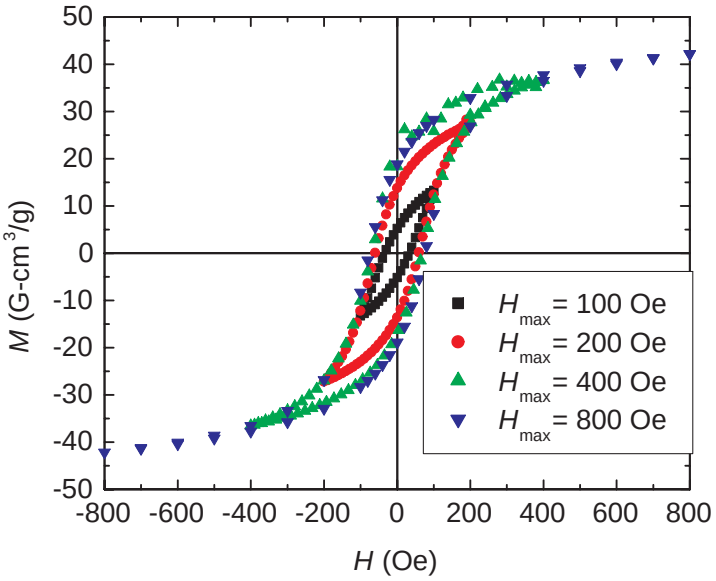

Figure 4.5: Hysteresis loop for Ni. The magnetization M vs. H for lossy, electroplated Ni at a temperature of 120 K. The plot illustrates that the FM Loss, $W = \int MdH$ = loop area, increases with H_{max}.

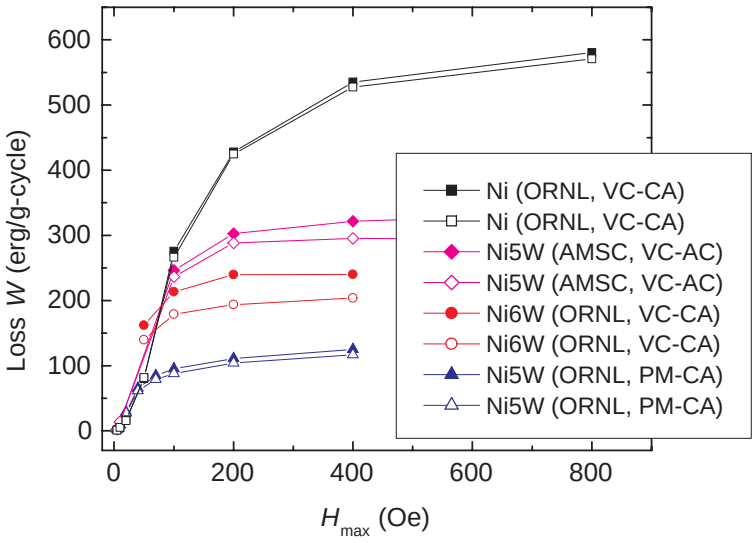

Figure 4.6: Hysteretic loss per cycle as a function of field excursion, for undeformed Ni, Ni-6at.%W and Ni-5at.%W. Measurements are taken at $T = 50$ K (filled symbols) or 77 K (open symbols). VC = vacuum cast; PM = powder metallurgy fabrication. CA = cut, then annealed; AC = annealed, then cut.

To better visualize some trends, we show in Fig. 4.7 the maximum ferromagnetic (FM) energy loss/cycle W for each alloy as biaxially textured (no bending deformation), at $T = 77$ K. In particular, the histogram contains values of loss measured in 400 Oe cycles, with the materials listed in order of increasing W-content. Two qualitative trends can be discerned. First, the loss W generally decreases when tungsten is added. This is hardly surprising, for Ni-W at these compositions forms a solid solution (no precipitates or inclusions that could pin domain walls) and, as shown in Fig. 4.2, the saturation magnetization M_{sat} decreases approximately linearly with W-content. The Ni-9at.%W has negligible loss, as expected from the critical concentration of W in Ni. Let us recall, however, the loss depends not only on intrinsic material properties like M_{sat}, but also on extrinsic features like the density of defects that pin domain walls. Second, then, we observe that the FM loss for materials with similar compositions tends to be lower for those annealed (recrystallized) at higher temperatures. For example, the Ni-5at.%W powder metallurgy material has lower loss than the vacuum cast Ni-6 at.%W alloy, where each was annealed - given its final heat treatment - after cutting to size (noted as "CA"). This second observation most likely originates from the higher annealing temperatures ($\sim$ 1300 ^{o}C) that could be used with the PM-based alloys (without inducing unwanted secondary recrystallization), compared with vacuum cast materials recrystallized near $\sim$ 1000 ^{o}C. Qualitatively, this should lead to a lower density of dislocations and related structural defects. Indeed, dislocations are reported to be a primary source of pinning that impedes domain wall motion in Ni [41] and one may expect similar effects in these dilute Ni-W alloys. Grain boundaries also act as pin domain walls, but the present materials are all strongly textured with small angle grain boundaries that constitute a "wall" of dislocation cores. With similar mean grain sizes, this implies that the differences between materials arise mostly from other features.

In practice, another source of defects in the materials is cutting, which creates localized damage near the severed edge. To assess this effect, we investigated the loss in Ni-5at.%W samples that were either cut-to-size (4 mm $\times$ 4 mm) first and then annealed ("CA") or annealed for recrystallization and then cut-to-size ("AC"). The results are shown in Fig. 4.8 as a plot of loss W versus H_{max}, all at $T = 77$ K.

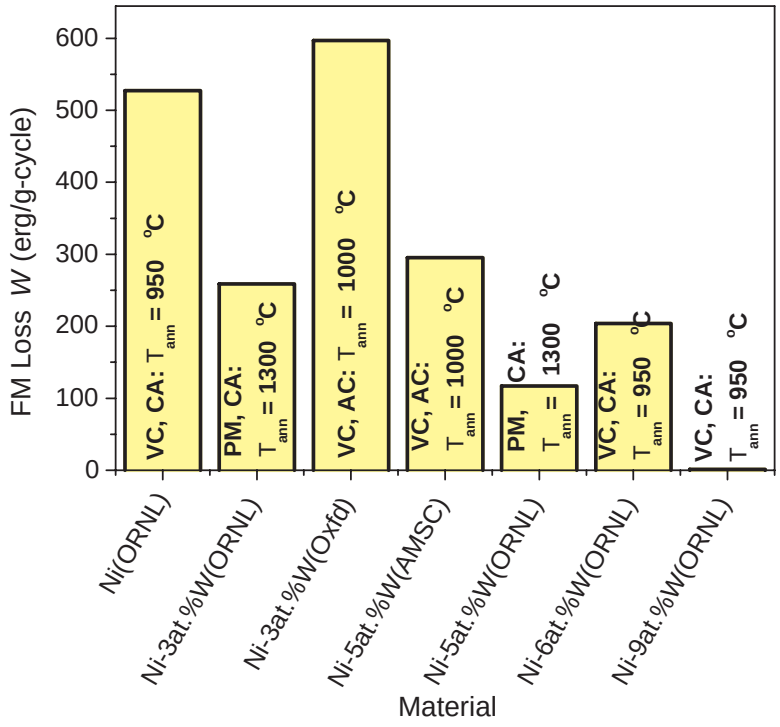

Figure 4.7: Histogram showing maximum hysteretic loss W of several samples. Alloys with same atomic composition have different values of FM losses due to different methods of preparation: alloys annealed at higher temperatures T_{ann} after cutting operations (CA) have lower FM losses; PM = Powder Metallurgy; VC = Vacuum Cast. Ni-9at.%W has an almost negligible loss.

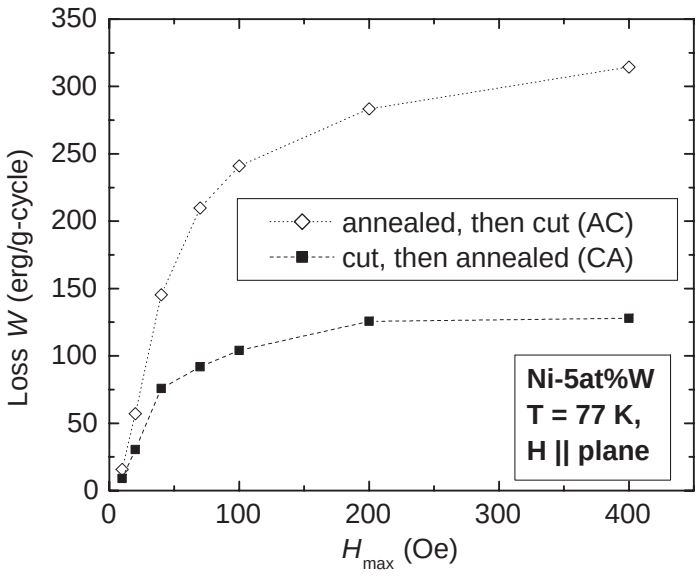

Figure 4.8: Effect of cutting on the ferromagnetic loss per cycle, shown as a function of field excursion H_{max}. The samples of undeformed Ni-5at.%W materials (prepared by vacuum casting, AMSC) were cut and then annealed (CA) or first recrystallized and then cut (AC).

Clearly, work-hardened edges induced by sample cutting significantly increased the ferromagnetic loss from its low initial level, e.g., increasing the coercive field H_c from 1 to 3 Oe. Losses in the vacuum-cast CA alloy are nearly identical to those measured in CA powder metallurgy alloys, all containing 5 at.% W. In a separate experiment, we cut a 4 mm $\times$ 4 mm CA sample into 3 pieces, severing it with a razor blade on a hard tungsten plate. This operation added 16 mm of freshly cut edges and added to the maximal loss at a rate of 1.2 erg/cycle per cm of cut edge (for this Ni-5at.%W material with 75 μm thickness). These combined results show that preparation and handling of the Ni-W alloy substrates play a prominent role in determining their hysteretic losses, as should be expected for this extrinsic property.

Next we consider the impact of bending deformation on the ferromagnetic loss/cycle. For this study, we used pure Ni, Ni-3at.%W and Ni-5at.%W materials. Each of these samples was deformed controllably by applying 0.4% bending strain, as described earlier.

Fig. 4.9 shows how the loss W increases with the number of half-cycles of bend, for Ni-3at.%W and Ni-5at.%W materials. This figure shows the maximal FM loss/cycle, as observed in field cycles with H_{max} = 400 Oe. For all alloys, the hysteretic loss increased with number of cycles of deformation, with the biggest jump in loss coming from the first half-step of deformation. A bending strain of 0.4 % lies near the limit tolerated by the superconductive coating in fully fabricated materials [42, 43]. We also applied 0.2 % and 0.7 % bending strains to a Ni-5%W sample from AMSC which was annealed after cutting. The result depicted in Fig. 4.10 shows similar trends observed for the 0.4 % strain measurements with the higher strained sample showing a greater loss W.

A check was made for adverse effects of temperature cycling, using a free-standing vacuum cast Ni-5at.%W sample as biaxially textured. Eight thermal cycles of T = 300 K - 77 K - 300 K changed the FM loss only slightly, from W = 295 to 302 erg/g-cycle. From this, we can say that FM loss is essentially unaffected by temperature cycling.

In ac magnetic measurements, a small oscillatory magnetic field is applied and the induced sample moment is time-dependent, unlike the dc measurements where the sample moment is constant during the measurement time. Such ac measurements can be very sensitive to small changes in $M(H)$. The ac susceptibility, $\chi = dM/dH$ is the (local) slope of the $M(H)$ curve and it is frequently the quantity of interest in ac magnetometry. More generally, however, a measurement of an ac magnetic moment yields two quantities: the magnitude of the moment $|m|$ and its phase shift φ, relative to the drive signal. Alternatively, one can consider the in-phase or real component m' and an out-of-phase, or imaginary, component m''. For ferromagnets, an irreversible domain wall movement appears as a finite dissipative component m''.

Values for the FM loss were obtained from the expression

$$W = \pi \times h_{ac} \times M'' \tag{4.1}$$

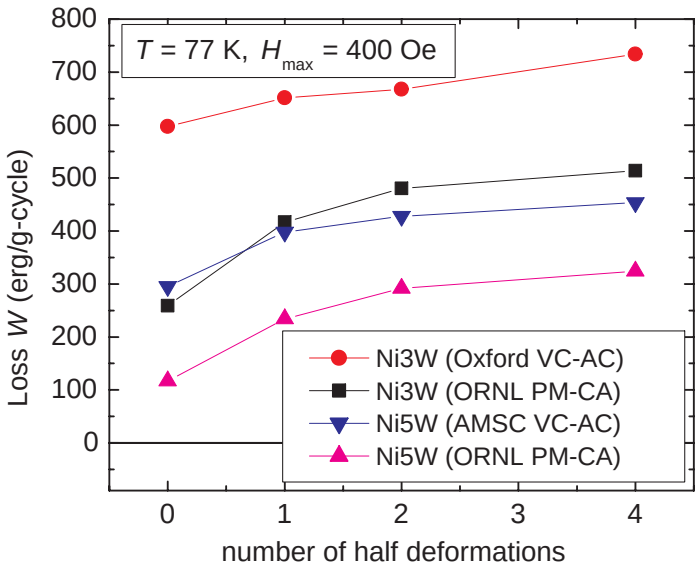

Figure 4.9: Hysteretic loss per cycle for Ni-3at.%W and Ni-5at.%W as a function of number of half-cycles of deformation. Loss increases with number of cycles of deformation (0.4% bending strain). VC = vacuum cast; PM = powder metallurgy; AC = recrystallized and cut-to-size; CA = cut-to-size and then annealed.

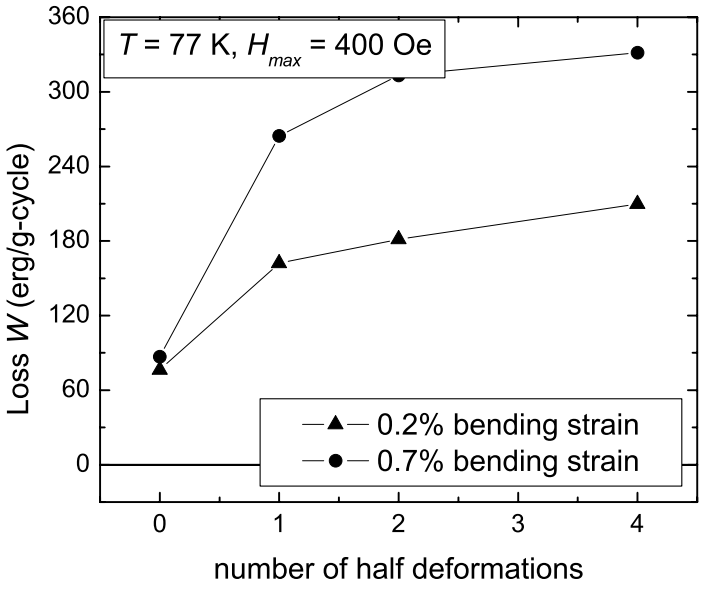

Figure 4.10: Hysteretic loss per cycle for Ni-5at.%W sample as a function of number of half-cycles of deformation for different bending strains. The bending strains applied are 0.2% and 0.7%. Similar features are observed as in the 0.4% strain.

where M'' is the out-of-phase mass magnetization and h_{ac} is the peak amplitude of the applied ac field [44]. The SQUID magnetometer provides an ac field up to 6.8 Oe and its frequency range is from 0.001 to 1000 Hz. Comparing experimental values for loss W from ac and dc measurements gave good agreement between the two methods, although this could only be done for small fields, up to 6.8 Oe.

We used this ac capability to investigate the relationship between the FM loss/cycle and the frequency of the applied field. This is important because some potential applications for coated conductors in specialized electrical equipment, e.g., airborne generators and devices, have operating frequencies well above the usual 50-60 Hz of the power grid. As seen in Fig. 4.11, the loss/cycle W was found to be independent of the ac field frequency, at least for the small fields that were used. The figure shows results for vacuum cast Ni-5at.%W at 77 K subjected to field amplitudes $h_{ac} = 4$ and 6.8 Oe, for frequencies f up to 600 Hz. Here, there was no dc bias field and the sample had no bending deformation. The significant increase in loss with $h_{ac} = 6.8$ Oe compared with that at $h_{ac} = 4$ Oe occurs when the field amplitude h_{ac} or H_{max} is comparable with the coercive field H_c. Another potential loss mechanism is from eddy currents, which gives a nominally frequency-dependent but amplitude-independent loss. However, we estimate the skin depth of this alloy to be several millimeters, much larger than the sample thickness, meaning that eddy losses should be small relative to the FM loss, as observed.

Finally, we investigated the effect of a dc bias field, H_{dc} on the FM loss W for a fixed ac field amplitude and frequency. Similar superpositioning of ac and dc magnetic fields may arise in applications, e.g., in the stator of a motor. Fig. 4.12 shows the result obtained for an undeformed Ni-5at.%W at h_{ac} of 5 Oe and temperature of 77 K. The loss decreased rapidly as the bias field H_{dc} increased and reduced W to nearly zero for a dc field of 50 Oe.

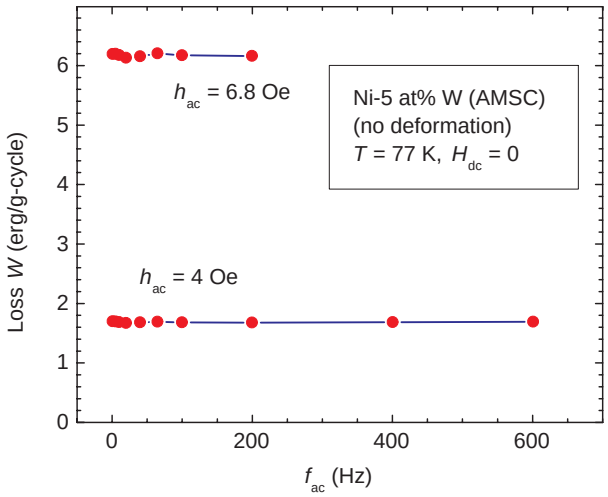

Figure 4.11: FM loss as a function of applied ac frequency. Two different fixed values of ac field are applied. Loss per cycle is independent of frequency in the range shown.

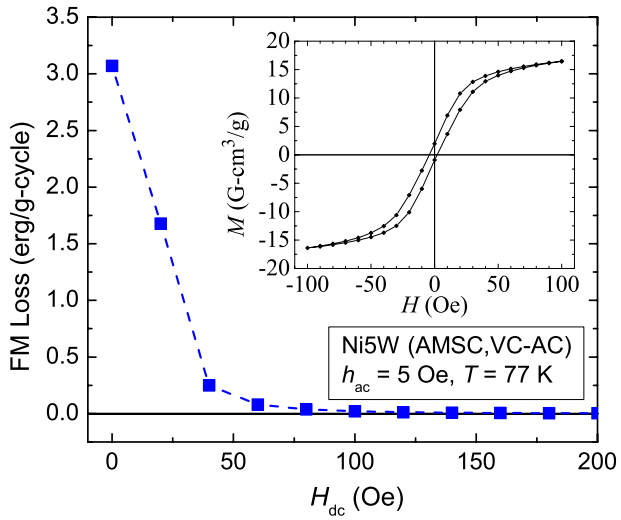

Figure 4.12: FM loss as a function of dc bias field. Hysteretic loss for undeformed Ni-5at.%W versus dc bias field at temperature of 77 K and a fixed ac field of 5 Oe. Loss decrease drastically when alloy is magnetized into reversibility by dc bias field. Inset: magnetization of similarly annealed-and-cut (AC) Ni5W alloy, showing that a field of 50 - 75 Oe drives the sample into a reversible state.

This is readily understood as a consequence of the fact that a dc field can magnetize the sample into its region of magnetic reversibility (and eventually saturation). For the lossy electroplated Ni in Fig. 4.5, this region corresponds to dc fields $>$ 400 Oe; it occurs at lower fields for the more reversible biaxially textured and annealed Ni-W alloys.

It is useful to provide some context for these FM properties of the substrate materials, by comparing their FM loss with the hysteretic loss expected from the superconductor itself when conducting an ac current. As an example, let us consider a RABiTS tape that is 4 mm wide with a 75 μm thick metal substrate, and has a YBCO coating on one side giving a critical current $I_c = 100$ A. To estimate the superconductive energy loss, we use the theory of Norris [18], which applies to a long isolated conductor with an I_c that is independent of field. The theory (for elliptic geometry) provides a reasonably good description of the ac loss in YBCO coated conductors on Ni [45], on Hastalloy [46], and on some NiW-based architectures[32]. For a peak ac current $I_0 = I_c$, the Norris expression gives a loss per cycle per meter (SI units) of $L_c = (1/2\pi)\mu_0 I_0^2 = 2$ mJ/m-cycle. For lower currents, Table 3 of Norris [45] shows that the losses are smaller by a factor of 3.2 at $I_0/I_c = 0.8$ and a factor of 9.4 at $I_0/I_c = 0.6$; the corresponding superconductive losses are $L_c = 0.63$ and 0.21 mJ/m-cycle, respectively.

In this example, each meter of tape contains 0.3 cm^3 = 2.7 g of alloy substrate. For illustration, we use data for the Ni-5 at%W alloy (CA) in Fig. 4.6. To obtain the approximate field amplitude H_{max}, we approximate the tape by a thin strip with a uniformly distributed current, which (away from the edges) creates a field $B = \mu_0 I_0/2w$ (SI units), where "w" is the tape width. This field is in the plane of the tape, i.e., with the same orientation as the quasi-static magnetic measurements. The resulting fields ($H_{max} = 126$ and 94 Oe) produce similar FM hysteretic losses (92 and 86 erg/g-cycle) of 0.025 and 0.023 mJ/m-cycle at $I_0/I_c = 0.8$ and 0.6, respectively. These FM losses constitute 4 % and 10 % of the total (superconductive plus ferromagnetic) loss at the respective current levels. The corresponding total dissipated power at 60 Hz is 122 mW/m at $I_0/I_c = 1$; 39 mW/m at the 0.8 level; and 14 mW/m at $I_0/I_c = 0.6$. For still lower current levels, the total power continues to decrease, while the FM loss becomes a progressively larger fraction of it.

This example illustrates the magnitude of losses that might be encountered in power line applications. Clearly the dissipated power will be larger at higher operating frequencies and with substrate materials that are deformed, cut, or otherwise damaged; on the other hand, both superconductive and FM losses could be reduced in conductor configurations with lower effective ac field amplitudes, e.g. possibly by grooving the conductor or coating both sides of the tape. Ultimately, the total loss will depend not only on the choice of substrate materials and operating conditions I_0/I_c, but also on the conductor and equipment layout that affects the ac field experienced by the conductor.

4.2 Critical Currents of YBCO Thin Films

4.2.1 Field Dependence of J_c

In the following analysis of the experimental results, we test the appropriateness and applicability of the Ivlev-Ovchinnikov-van der Beek formulation [25, 26] as summarized in Sec. 2.4.2. In particular, we ask whether it can describe J_c and the characteristic fields with values for the defect size and density that are comparable with the TEM observations for these materials. We start our discussion by considering the field dependence of J_c at the various temperatures studied. Fig. 4.13 and Fig. 4.14 show representative results J_c vs H, for films of several different thicknesses. The first observation is that in all cases, there is a low field region of single vortex pinning, where J_c is indeed nearly independent of H as described by Eq. 2.31. In Fig. 4.15 is shown the temperature dependence of H^* for several films as the temperature increases. H^* is the field at which the $J_c(H)$ curves start to deviate from non dependence (single vortex limit). As the temperature decreases, the values first rise and then become nearly constant in the range 50 - 30 K, with similar values for all thicknesses. For $T \leq 20$ K, H^* abruptly rises, which may originate in additional pinning from point-like defects that are relatively ineffective at higher temperatures. Thus we focus on the region $T \geq 30$ K, where H^* varies from ~ 0.12 T at 30 K to ~ 0.04 T at 77 K.

From Eq. 2.34 and the preceding discussion, we have $H^* \sim ln[1 + D_i^2/2\xi^2(T)]$. From Ginzburg-Landau theory, the coherence length ξ is $\xi^2(T) = \frac{\hbar}{|2m^*\alpha(T)|}$

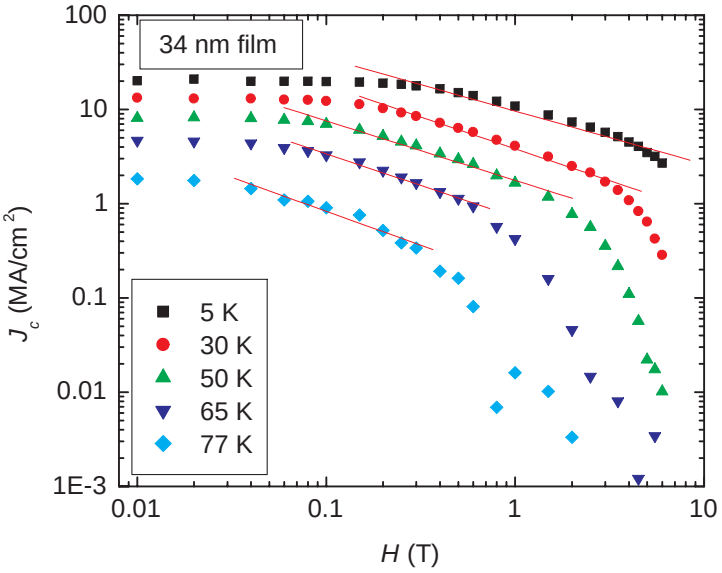

(a)

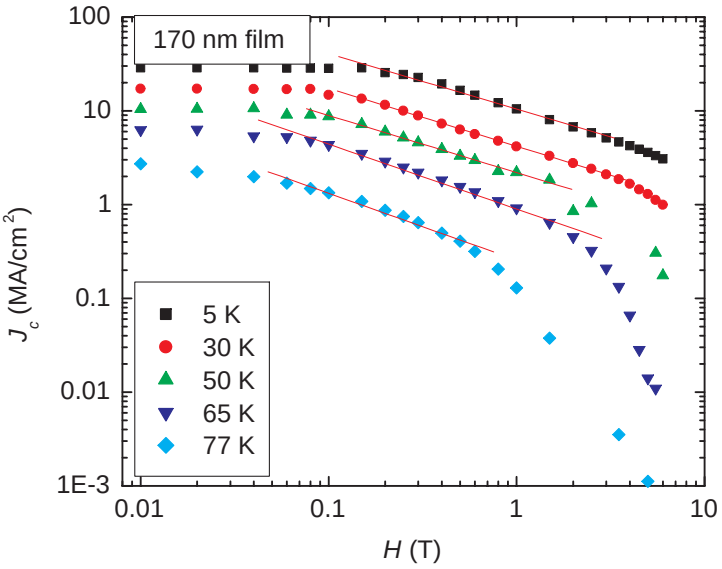

(b)

Figure 4.13: Field dependence of the critical current density J_c for a 34 and 170 nm thick film. From the lines drawn on each set of data, we obtain the exponent β in $J_c \propto H^{-\beta}$ in the intermediate field range. For all the materials, $\beta \sim 0.56$ - 0.69. (a) 34 nm thick film (b) 170 nm thick film.

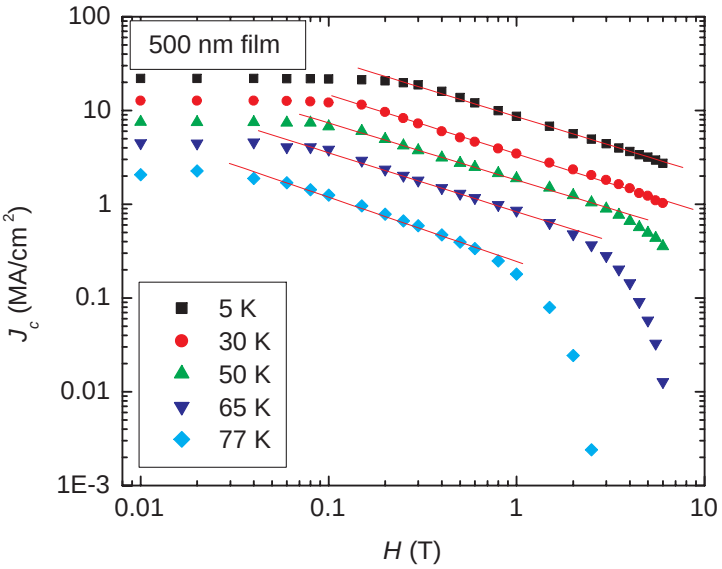

(a)

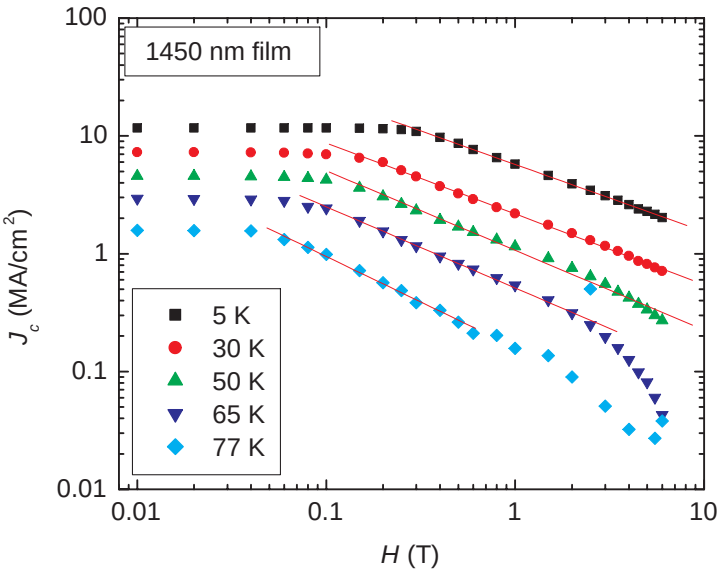

(b)

Figure 4.14: Field dependence of the critical current density J_c for a 500 and 1450 nm thick film. From the lines drawn on each set of data, we obtain the exponent β in $J_c \propto H^{-\beta}$ in the intermediate field range. For all the materials, $\beta \sim 0.56$ - 0.69. (a) 500 nm thick film (b) 1450 nm thick film.

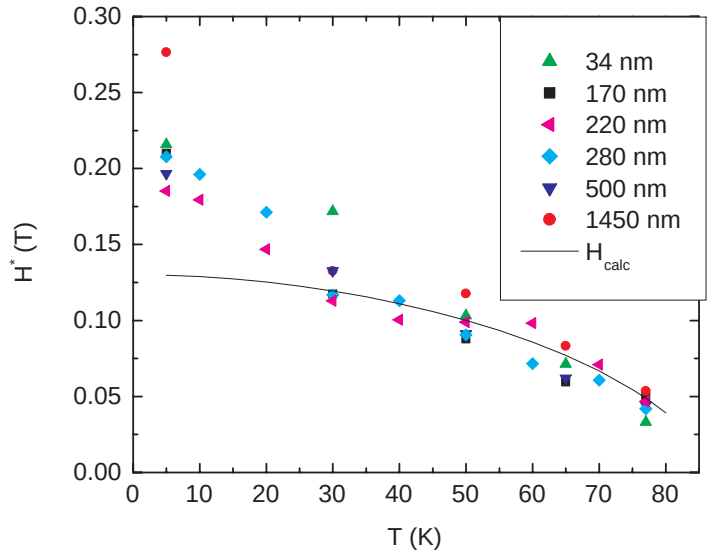

Figure 4.15: Variation of the cross-over field H^* with temperature. Data are for films of thicknesses from 34 to 1450 nm. Drawn line is the theoretical prediction.

where $\alpha(T) \propto (1 - T/T_c)$ near T_c is a temperature dependent parameter. This temperature dependence, shown as a solid line in Fig. 4.15, gives a reasonable description of the data at intermediate and higher temperatures, taking $D_i^z = 10$ nm both for this temperature dependence and for self consistency with the magnitude of J_c, as discussed below. Then with $H^* = 0.12$ T as appropriate for most of the films at moderate temperatures 30 - 50 K, the expression Eq. 2.34 for H^* yields a defect density $n_i = 2.4 \times 10^{21}$ m^{-3}. In the same low-field limit, we alternatively calculate from Eq. 2.31 (again with $D_i^z = 10$ nm) and the experimental $J_c \approx 15 \times 10^6$ A $\cdot$ cm^{-2} and obtain $n_i = 3.1 \times 10^{21}$ m^{-3}. These estimates are reasonably consistent internally and comparable with the defect density of 4.8×10^{21} m^{-3} obtained directly from the TEM study, to be discussed in Sec. 4.2.4.

A particularly interesting feature in the $J_c(H)$ data in Fig. 4.13 and Fig. 4.14 occurs in the intermediate field range. There the current density falls off with a power law field dependence $J_c \propto H^{-\beta}$ with exponent $\beta \sim$ (0.56 - 0.69) for all the materials studied. This power law coincides closely with the prediction of Ovchinnikov and Ivlev [25], who obtain in

Eq. 2.32 for $J_c(H)$ that $\beta = 5/8$ (0.625). As for the *magnitude* of J_c estimated from Eq. 2.32, the values obtained (using the same defect density and size described above) exceed those measured in these YBCO thin films by about a factor of 20. This overestimation of J_c has been attributed [26] to an assumption that a vortex line will encounter at least one defect (more explanations in footnote 27 in Ref. 26). In addition, the presence of some weak links also reduces somewhat the current densities below the levels expected in equivalent single crystal films, as the present materials are realistically quasi-single crystals consisting of a series-parallel network of predominantly low angle grain boundaries. However, for high quality coated conductors such as those studied here, the attenuation in J_c is typically a factor-of-2 or less and cannot account for the difference in estimated versus experimental J_c values.

Similar difficulties arise with numerical estimates of the crossover field H_a, separating the $\beta \sim 5/8$ and the $\beta \sim 1$ regions in the Ivlev-Ovchinnikov theory. Estimates in the range of 10^{-3} T are obtained, compared with experimental values of 1 - 3 T.

For complementary estimates, we turn to the alternative, simpler development leading to Eq. 2.35 and Eq. 2.36. In this case, the theoretical power law dependence with $\beta = 1/2$ is slightly weaker than either the Ivlev-Ovchinnikov theory or the experimental findings. On the other hand, the magnitude of the current density lies much closer to that realized experimentally. From Eq. 2.35, we obtain $J_c \approx 19$ MA/cm$^2\times$ (1 T/B)$^{1/2}$ again using the same defect parameters $n_i = 3 \times 10^{21}$ m^{-3} and $D_z^i = 10$ nm. The resulting estimate for J_c lies within about a factor-of-3 of the experimental values, which is relatively good agreement for such estimates. One may also evaluate the cross-over field $\widetilde{B}_a$ separating regions with power law behavior with $\beta = 1/2$ and $\beta = 1$, using Eq. 2.36. This leads to the estimate $\widetilde{B}_a \approx 1.4$ T, which is close to the experimental values in Fig. 4.13 and Fig. 4.14 for the several films of various thicknesses. Finally, as we approach the irreversibility line (where the films lose their ability to carry any significant amount of supercurrent), $J_c(H)$ collapses progressively more quickly with increasing temperatures.

4.2.2 Thickness Dependence of J_c

Useful, complementary information can be obtained from the dependence of J_c on film thickness d. Understanding this dependence is vital to gaining insights for improving the total current carrying capabilities of a CC. It is widely recognized that for thicker films, the experimental J_c decreases as thickness is increased; this has been attributed, at least in part, to bad film morphologies and/or differences in defect structure between the thinner and the thicker films. [47]. One potential way to circumvent this problem is based on extrapolating the $J_c(d)$ dependence to very thin films, which implies extremely high J_c values; then could fabricating a stack of very thin layers lead to a very high overall J_c? On the other hand, might materials - related problems lead to very small J_c in thin films on RABiTS? These are some of the motivations for undertaking this study.

Although extensive studies have been reported to investigate the d-dependence of J_c in YBCO thick films on single crystalline and buffered metallic substrates [48] as well as for thin films on single crystalline substrates [26], no work has been reported for thin films on buffered (RABiTS) substrates. From our results, the $J_c(d)$ data can be divided into two regions viz: thin -thin films and thick thin films. In Fig. 4.16 is shown a plot of the experimental $J_c(d)$ measured in self - field; in the first region of "thin thin films" described by Eq. 2.37, we find that J_c first increases with thickness d; it then reach a peak around $\sim$ 120 - 140 nm and decrease thereafter. This behavior is independent of temperature as the same effect is found at low (5 K) and high (77 K) temperature. Furthermore, similar plots in Fig. 4.17 for applied fields of 2 and 5 kOe fields reveal the same features found in the self - field data. This temperature independence implies that the thickness where the peak J_c occurs is not directly related for these materials to the value for the penetration depth λ_{ab}, as reported in an earlier work [48]. In addition, the similarity of $J_c(d)$ at high and low temperatures also argues against explanations based on thermal depinning of thickness-limited vortex segments to account for the decreased J_c observed in the thinnest films.

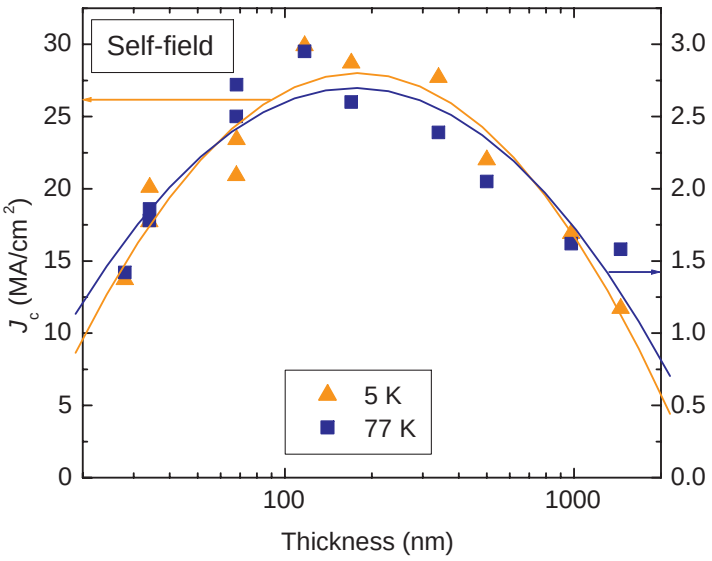

Figure 4.16: Thickness dependence of J_c in self field. A semi log plot of $J_c(d)$ shows that J_c increases initially with thickness, attain a peak, then decreases thereafter. This feature is seen in both the 5 K and 77 K data. Here, there is no applied field.

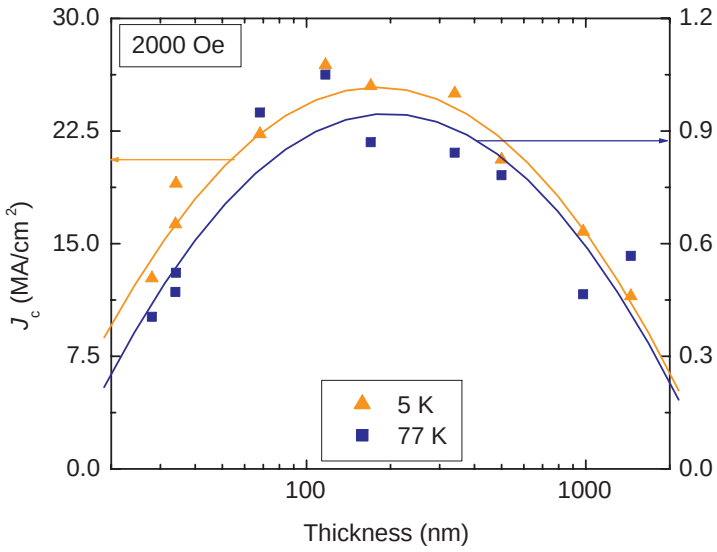

(a)

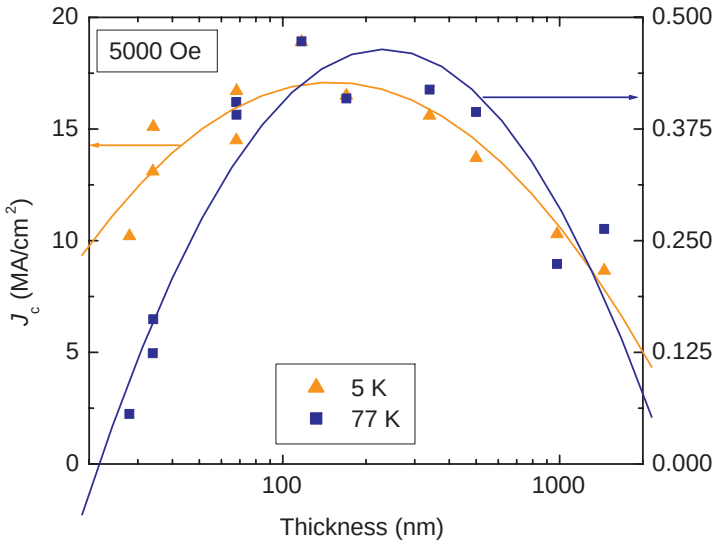

(b)

Figure 4.17: Thickness dependence of J_c in an applied field H. (a) shows the result for a field of 2 kOe while (b) is that for $H = 5$ kOe. The peak J_c is at the same thickness d of the films in both cases.

Continuing, the theory predicts a linear dependence of J_c on d in the thin-thin region, as seen in Eq. 2.37. Examination of the experimental data in Fig. 4.18 for T = 5 K and T = 77 K reveals an initial linear rise in J_c as shown by the dashed lines; with further increases in thickness, the J_c dependence rolls over and peaks near 120 nm, as discussed above. In the thin-thin region, the experimental data have a slope at low temperature of $J_c/d = 5.7 \times 10^{18}$ A/m^3, which can be compared to the theoretical value $n_i D_i^z F(T) U_p / \Phi_0 \epsilon^2 4\xi$ predicted by Eq. 2.37. This yields for the defect density a value $n_i = 1 \times 10^{21}$ m^{-3}, which is roughly consistent with the values obtained in earlier analyses of the $J_c(H)$ relationship and the cross-over field in the single vortex limit. Lastly, using this latter value n_i in Eq. 2.38 gives a crossover film thickness $d^* \approx 40$ nm, which lies near the thickness where the $J_c(d)$ data depart from their initial linear dependence.

4.2.3 Temperature Dependence of J_c

In type II superconductors, pinning results from spatial variations of the Ginsburg-Landau (GL) coefficient α associated with disorder in the T_c and/or from spatial variations in the charge carrier mean free path l near lattice defects. These two sorts of pinning are usually called "δT_c *pinning*" and "δl *pinning*", respectively [49]. The type of pinning in high T_c superconducting materials can give insights into the vortex structure as each of them is governed by different regimes of the GL free energy functional [50]. In the single vortex regime, which is the region of interest in this analysis, J_c can be expressed as a function of the reduced temperature $t = (T/T_c)$ as:

$$J_c(t) \approx (1 - t^2)^{7/6} \tag{4.2}$$

$$J_c(t) \approx (1 - t^2)^{5/2} \tag{4.3}$$

Eq. 4.2 holds for "δT_c *pinning*" while Eq. 4.3 holds for "δl *pinning*" . In Fig. 4.19 and Fig. 4.20, we present the J_c in self field as a function of temperature normalized to the T_c for the 34, 117, 500 and 1450 nm thick films. These results are representative of all the

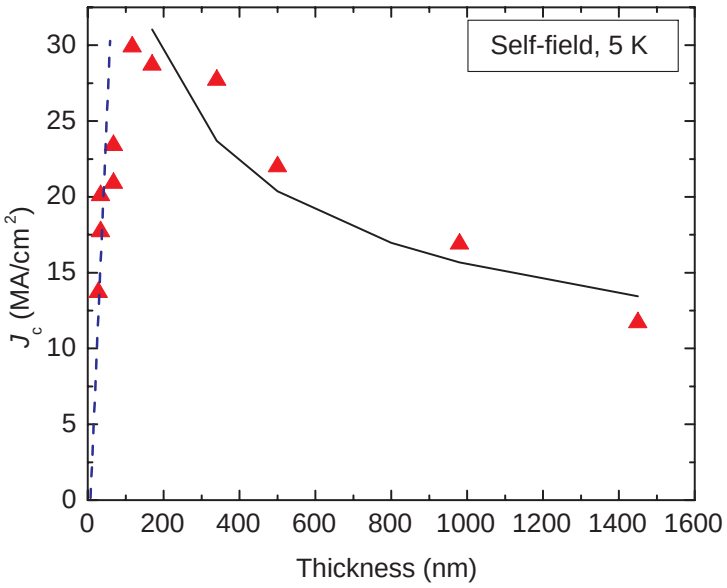

(a)

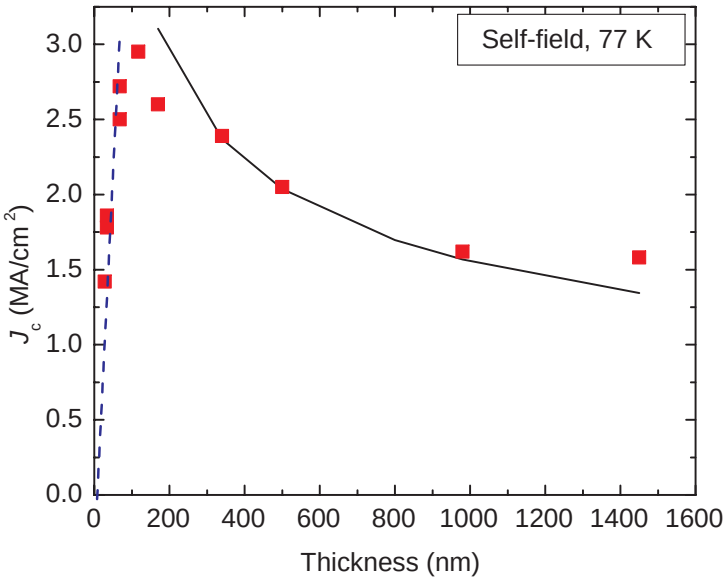

(b)

Figure 4.18: Plot of J_c vs d. J_c values are at self - field and T = 5 K. The solid line is a $d^{-0.4}$ fit to the data in the thick- thin film region. (b) The same, now for T = 77 K data.

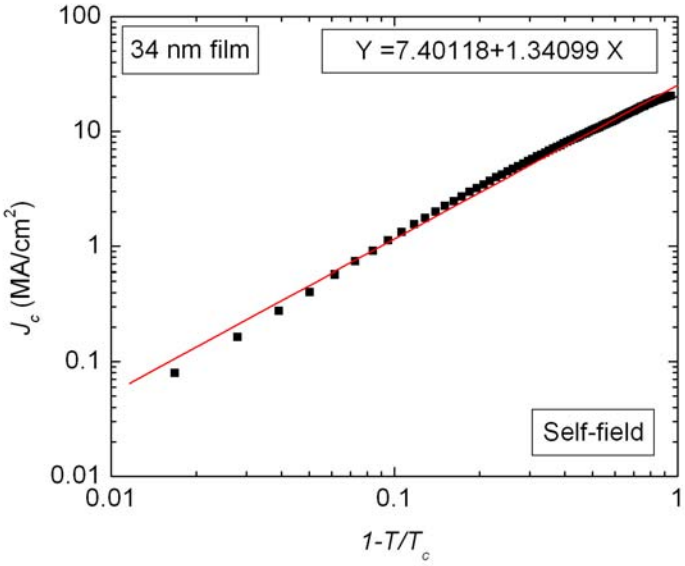

(a)

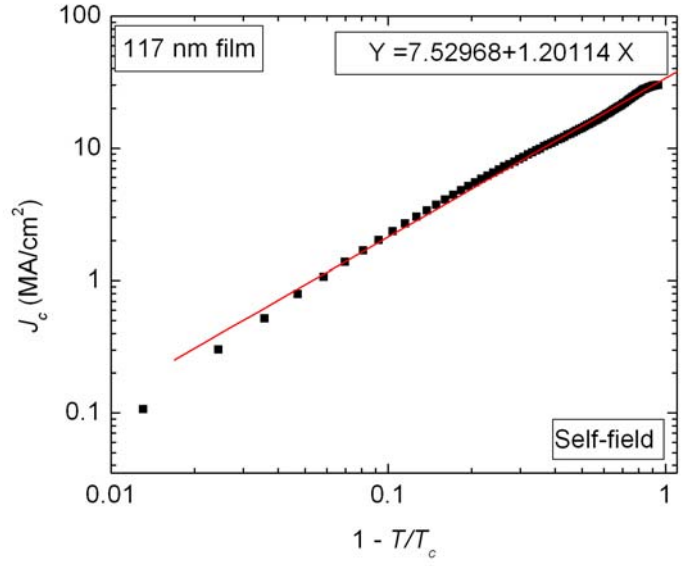

(b)

Figure 4.19: Temperature dependence of J_c in self field for a 34 and 117 nm thick film. Log-log plot of J_c vs $1 - T/T_c$ to show the temperature dependence. J_c values are those at self - field in order to ensure single vortex regime. Straight lines drawn are the best fits used to obtain the slopes. From theoretical models, values of slope point to "δT_c *pinning*" for all these materials. (a) 34 nm film (b) 117 nm film.

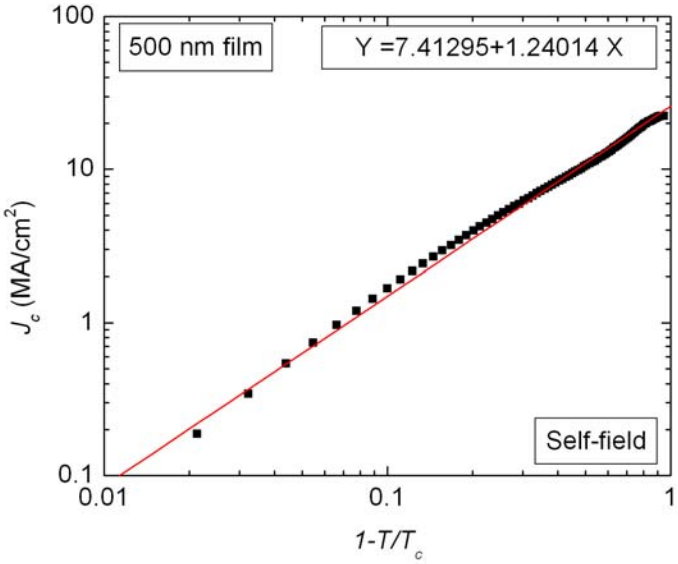

(a)

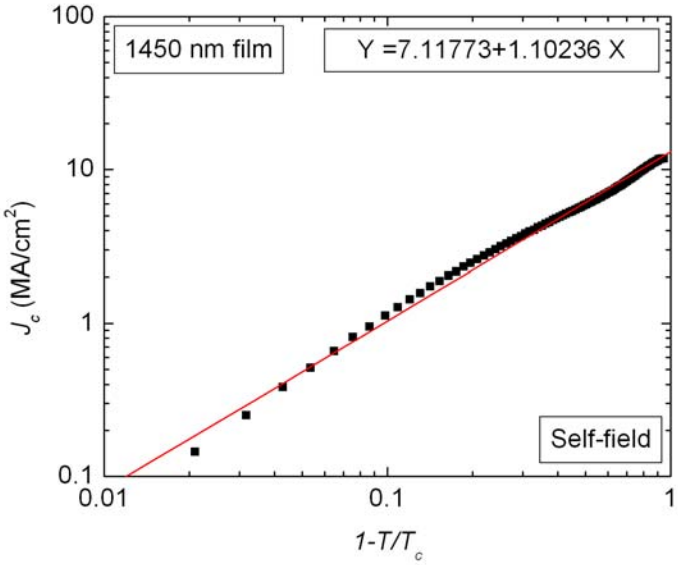

(b)

Figure 4.20: Temperature dependence of J_c in self field for a 500 and 1450 nm thick film. Log-log plot of J_c vs $1 - T/T_c$ to show the temperature dependence. J_c values are those at self - field in order to ensure single vortex regime. Straight lines drawn are the best fits used to obtain the slopes. From theoretical models, values of slope point to "δT_c *pinning*" for all these materials. (a) 500 nm film and (b) 1450 nm film.

films. The log-log plots of J_c vs $(1 - T/T_c)$ have slopes near T_c that range from 1.1 to 1.3. These values coincide within experimental error with the theoretical exponent 7/6 in the theoretical model Eq. 4.2 for "δT_c *pinning*". This finding of "δT_c *pinning*" is entirely consistent with the observed large precipitates of Y_2O_3, Y-Cu-O, etc. in the materials, as these insulating precipitates are completely non-superconductive. TEM images of these precipitates are shown in the next section.

4.2.4 TEM Images

In order to see detailed microscopic features of the films, collaborative transmission electron microscopy (TEM) studies were performed on representative samples by X. Song at the University of Wisconsin, Madison. The TEM images were taken looking from above, along the axis of film deposition (plan-view images). The images revealed various secondary phases in the YBCO films, from which their size distribution and density were determined. In addition to the secondary phases of Y_2O_3 and Y-Cu-O present in the films, there are also twin spacing in the range of 35 to 50 nm and large spherical pores faceted along the (110) and (100) planes of YBCO grains. Fig. 4.21 shows the TEM image from the 117 nm thick film while Fig. 4.22 shows that from the 340 nm thick film. An analysis of the defect sizes revealed a roughly log-normal distribution, with $\sim 2/3$ of the particles having diameters in the range (28 ± 11) nm. The density of defects is approximately 4.8×10^{21} m^{-3}. These values are typical of the materials in this series and corroborate the preceding analysis of pinning by large sparse defects.

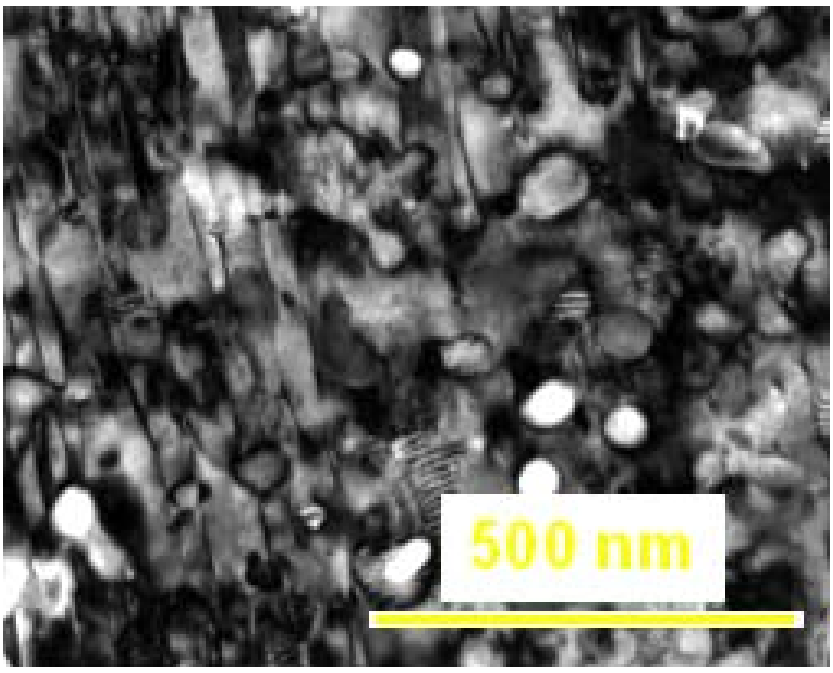

Figure 4.21: A TEM image of the 117 nm thick film.

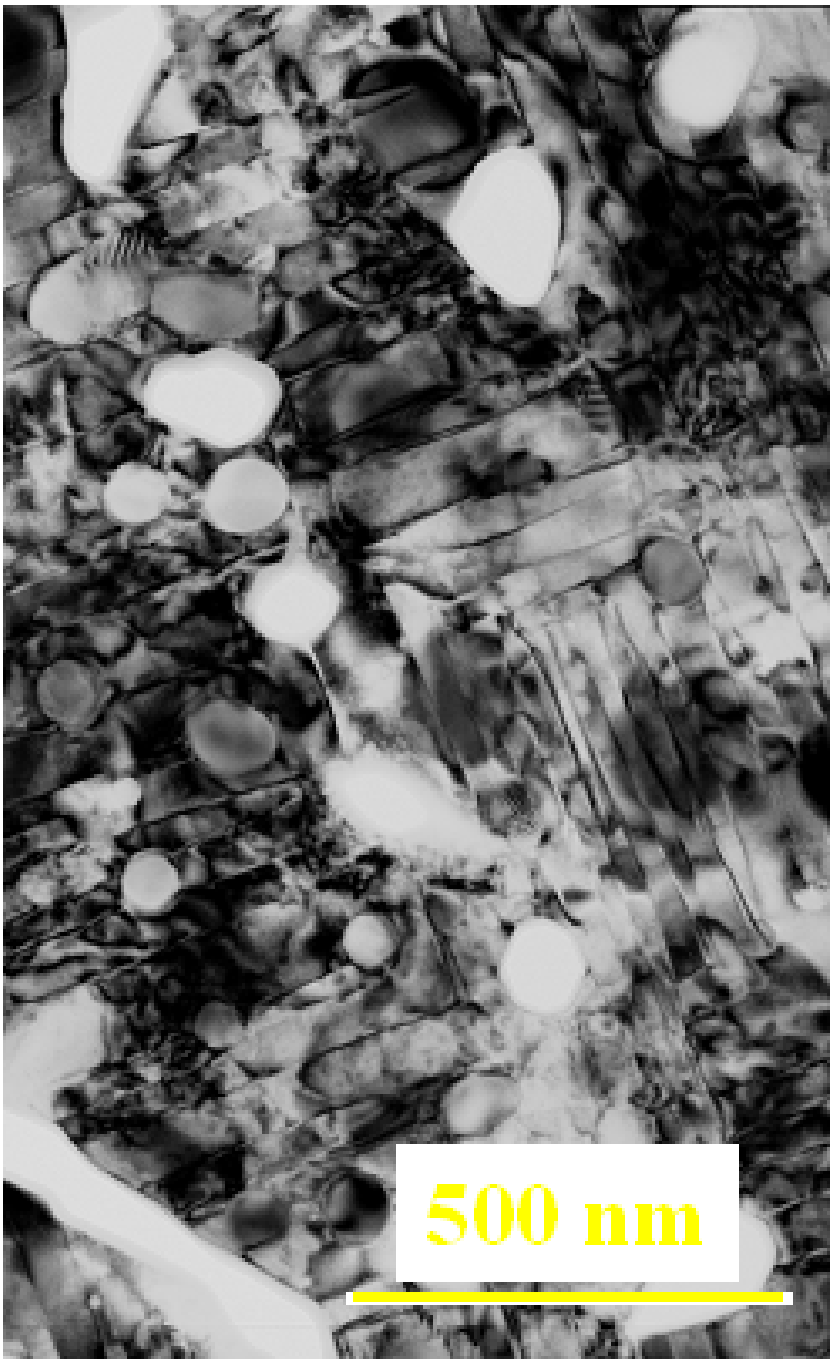

Figure 4.22: A TEM image of the 340 nm thick film.

Chapter 5

Conclusions

Coated conductors based on $YBa_2Cu_3O_{7-\delta}$ (YBCO) are being developed as second generation high temperature superconducting wires, with steady progress on issues such as limitations on the critical current density J_c arising from weak links at grain boundaries. This problem of low J_c due to improper alignment of the grains is being circumvented by depositing the superconducting films on well textured substrates. The "RABiTS" technique is one of the methods presently used to deposit the YBCO films on well textured Ni alloys substrates. These substrates are ferromagnetic (FM), hence they contribute to the overall ac loss in the coated conductor. We have studied the FM properties and FM loss of Ni-W alloys (one of the choice alloys) extensively and showed factors that contribute to their being lossy.

Substrate materials $Ni_{1-x}W_x$ alloys with x = 0, 3, 5, 6, and 9 at.% W were studied. The alloys were produced by either vacuum cast or powder metallurgy method. From saturation magnetization (M_{sat}) and Curie temperature (T_c) measurements, the critical concentration of W in Ni was found to be $\approx$ 9.5 at.%. The ferromagnetic (FM) loss measured for these alloys first increases approximately linearly with field excursion and then saturates at larger H_{max}. FM loss, being an extrinsic property, depends on the handling and methods of preparation of the alloys. This loss increases with bending deformation

(due to pinning of domain walls by induced defects) and also alloys that were recrystallised at lower temperatures during processing have higher losses.

From ac studies, we found that FM loss is independent of frequency up to about 600 Hz and it decreases drastically when alloy is saturated by a dc bias field.

The effect of magnetic relaxation in HTSC arise due to the motion of vortices. In order to have high values of J_c, vortices have to be well pinned, i.e., made immobile. Understanding the physics of vortices can help in explaining the thickness dependence of J_c in the YBCO films. J_c tends to rise at first as the films are made thicker, but falls off after reaching a particular thickness. The relationship between the J_c and the applied field can give an insight into the type of vortex pinning in superconductors. Also, via a collaboration with our colleagues, we investigated the microstructure of these YBCO films by probing with Transmission Electron Microscope (TEM). The TEM analysis helped us evaluate the microstructural features in the bulk of the films.

We have studied the pinning mechanisms and the dependencies of J_c on film thickness, field and temperature in thin *ex-situ* YBCO films deposited on buffered RABiTS substrates of Ni-5%W. While comparing experimental results with theoretical predictions, we identified the dominant pinning mechanism in these YBCO materials to be from strong pinning by large defects. This conclusion was corroborated by images from TEM. Plan-view images of some of our samples show various secondary phases of Y_2O_3 and Y-Cu-O, as well as twins. Furthermore, the density of the defects counted by hand from the TEM images agree reasonably well with estimates from theoretical predictions.

From the thickness dependent studies, we found that J_c increases initially with thickness, reaches a peak at about 120 nm and then fall off. Reasonably high values of J_c were also measured in these films; hence, we conclude that material-related problems are not a major issue when it comes to these thin films on RABiTS. Furthermore, these results suggest that using a thicker layer of YBCO on RABiTS substrates to improve the overall current capacity of a CC may be promising, as the falloff of J_c with thickness is not as fast as observed earlier.

Results obtained from the field dependent studies also show that the defects that allow for pinning in these materials are large and sparsely distributed, as treated in theories based on strong pinning.

Looking ahead, we still need better theoretical guidance on the thickness dependence of J_c in order to understand better the falloff in thicker films and to devise more effective methods in fabricating thick films with reasonably high values of J_c.

In the coming decade, high-temperature superconductors will revolutionize much of industry and technology. While the initial euphoria in the field of superconductivity was related to the discovery of new superconductor "systems" and compounds, recent efforts are geared towards developing innovative fabricating methods in order to increase the levels of J_c conducted by these materials. We have undertaken this study in order to get a better understanding of the basic phenomena of superconductivity in these materials and more precisely, to understand ways to improve the magnetic quality of these materials by enhancing flux pinning in a controllable manner.

References and Bibliography

References

1. H. K. Onnes, Leiden Comm. B **120** (1911).

2. J. G. Bednorz and K.A. Muller, Z. Phys. B **64**, 189 (1986).

3. C. W. Chu, P. H. Hor, R. L. Meng, L. Gao, Z. J. Huang, and Y. Q. Wang, Phys. Rev. Lett. **58**, 405 (1987).

4. J. E. Kunzler, E. Buehler, F. S. L. Hsu, and J. H. Wernick, Phys. Rev. Lett. **6**, 89 (1961).

5. D. Larbalestier, A. Gurevich, D. M. Feldmann, and A. Polyanskii, Nature **414**, 368 (2001).

6. D. P. Norton, A. Goyal, J. D. Budai, D. K. Christen, D. M. Kroeger, E. D. Specht, Q. He, B. Saffian, M. Paranthaman, C. E. Klabunde, D. F. Lee, B. C. Sales, and F. A. List, Science **274**, 755 (1996).

7. A. Goyal, D. P. Norton, D. K. Christen, E. D. Specht, M. Paranthaman, D. M. Kroeger, J. D. Budai, Q. He, F. A. List, R. Feenstra, H. R. Kerchner, D. F. Lee, E. Hatfield, P. M. Martin, J. Mathis, and C. Park, Appl. Superconduct. **4**, 403 (1996).

8. M. W. Rupich, U. Schoop, D. T. Verebelyi, C. Thieme, W. Zhang, X. Li, T. Kodenkandath, N. Nguyen, E. Siegal, D. Buczek, J. Lynch, M. Jowett, E. Thompson, J. S. Wang, J. Scudiere, A. P. Malozemoff, Q. Li, S. Annavarapu, S. Cui, L. Fritzemeier, B. Aldrich, C. Craven, F. Niu, R. Schwall, A. Goyal, and M. Paranthaman, IEEE Trans. Appl. Supercond. **13**, 2459 (2003).

9. C. P. Wang, K. B. Do, M. R. Beasley, T. H. Geballe, and R. H. Hammond, Appl. Phys. Lett. **71**, 2955 (1997).

10. J. R. Groves, P. N. Arendt, S. R. Foltyn, R. F. DePaula, C. P. Wang, and R. H. Hammond, IEEE Trans Appl. Supercond. **9**, 1964 (1999).

11. K. Hasegawa, K. Fujino, H. Mukai, M. Konishi, K. Hayashi, K. Sato, S. Honjo, Y. Sato, H. Ishii, and Y. Iwata, Appl. Superconduct. **4**, 487 (1996).

12. U. Balachandran, M. Li, R. E. Koritala, B. F. Fisher, and B. Ma, Physica C **372**, 869 (2002).

13. T. Aytug, M. Paranthaman, J. R. Thompson, A. Goyal, N. Rutter, H. Y. Zhai, A. A. Gapud, A. O. Ijaduola, and D. K. Christen, Appl. Phys. Lett. **83**, 3963 (2003).

14. J. R. Thompson, A. Goyal, D. K. Christen, and D. M. Kroeger, Physica C **370**, 169 (2001).

15. A. O. Ijaduola, J. R. Thompson, A. Goyal, C. L. H. Thieme, and K. Marken, Physica C **403**, 163 (2004).

16. L. Civale, A. D. Marwick, T. K. Worthington, M. A. Kirk, J. R. Thompson, L. Krusin-Elbaum, Y. Sun, J. R. Clem, and F. Holtzberg, Phys. Rev. Lett. **67**, 648 (1991).

17. J. L. MacManus-Driscoll, S. R. Foltyn, Q. X. Jia, H. Wang, A. Serquis, L. Civale, B. Maiorov, M. E. Hawley, M. P. Maley, and D. E. Peterson, Nature Materials **3**, 439 (2004).

18. W. T. Norris, J. Phys. D: Appl. Phys. **3**, 489 (1970).

19. P. Weiss, J. Phys. **6**, 661 (1907).

20. P. Weiss and R. Forrer, Ann. Phys. **5**, 153 (1926).

21. W. Meissner and R. Ochsenfeld, Naturwissenschaften **21**, 787 (1933).

22. F. London and H. London, Proc. Roy. Soc.(London) **A149**, 71 (1935).

23. V. L. Ginzburg and L. D. Landau, Zh. Eksperim. i Teor. Fiz. **20**, 1064 (1950).

24. A. I. Larkin and Y. N. Ovchinnikov, J. Low Temp. Phys. **21**, 409 (1979).

25. Y. N. Ovchinnikov and B. I. Ivlev, Phys. Rev. B **43**, 8024 (1991).

26. C. J. van der Beek, M. Konczykowski, A. Abal'oshev, I. Abal'osheva, P. Gierlowski, S. J. Lewandowski, M. V. Indenbom, and S. Barbanera, Phys. Rev. B **66**, 024523 (2002).

27. P. H. Kes and C. C. Tsuei, Phys. Rev. Lett. **47**, 1930 (1981).

28. V. M. Vinokur, B. Khaykovick, E. Zoldov, M. Konczykowski, R. A. Doyle, and P. H. Kes, Physica C **295**, 207 (1998).

29. C. P. Bean, Phys. Rev. Lett. **8**, 250 (1962).

30. C. P. Bean, Rev. Mod. Phys. **36**, 31 (1964).

31. A. M. Campbell and J.E. Evetts, Advances in Physics **21**, 199 (1972).

32. R. C. Duckworth, J. R. Thompson, M. J. Gouge, J. W. Lue, A. O. Ijaduola, D. Yu, and D. T. Verebelyi, Supercond. Sci. Technol. **16**, 1294 (2003).

33. R. Feenstra, "The BaF_2 method: A scalable process for YBCO coated conductors," presented at the US Dept. of Energy Wire Development Workshop, St. Petersburg FL, Jan 29-30, 1998.

34. Y. Zhang, R. Feenstra, J. R. Thompson, A. A. Gapud, T. Aytug, P. M. Martin, and D. K. Christen, Supercond. Sci. Technol. **17**, 1154 (2004).

35. B. D. Josephson, Phys. Letters **1**, 251 (1962).

36. M. J. Besnus, Y. Gottehrer, and G. Munshy, Phys. Stat. Sol. B **49**, 597 (1972).

37. V. Marian, Ann. Phys. Ser. 11, **7**, 459 (1937).

38. R. P. Bozorth, *Ferromagnetism* (IEEE Press, Piscataway, NJ, 1978), pp. 325-6.

39. Landolt-Boernstein New Series Group III, vol. 19a, *Magnetic Properties of Metals* edited by M. Shiga (Springer-Verlag, Berlin, 1989), p. 563.

40. N. W. Ashcroft and N. D. Mermin, *Solid State Physics* (Holt, Rinehart and Winston, New York, 1976), p. 699.

41. V. A. Demkin, Phys. Stat. Sol. (a) **128**, 375 (1991).

42. C. Park, D. P. Norton, J. D. Budai, D. K. Christen, D. Verebelyi, R. Feenstra, D. F. Lee, A. Goyal, D. M. Kroeger, and M. Paranthaman, Appl. Phys. Lett. **73**, 1904 (1998).

43. C. L. H. Thieme, E. Fleshler, D. M. Buczek, M. Jowett, L. G. Fritzemeier, P. N. Arendt, S. R. Foltyn, J. Y. Coulter, and J. O. Willis, IEEE Trans. Appl. Supercond. **9**, 1494 (1999).

44. J. R. Clem and A. Sanchez, Phys. Rev. B **50**, 9355 (1994).

45. H. R. Kerchner, D. P. Norton, A. Goyal, J. D. Budai, D. K. Christen, D. M. Kroeger, E. D. Specht, Q. He, M. Paranthaman, D. F. Lee, B. C. Sales, F. A. List, and R. Feenstra, Appl. Phys. Lett. **71**, 2029 (1997).

46. M. Ciszek, O. Tsukamoto, N. Amemiya, J. Ogawa, O. Kasuu, H. Ii, K. Takeda K, and M. Shibuya, IEEE Trans. Appl. Supercond. **10**, 1138 (2000).

47. Ch. Jooss, A. Forkl, R. Warthmann, H-U Habermeier, B. Leibold, and H. Kronmuller, Physica C **266**, 235 (1996).

48. S. R. Folytn, P. Tiwari, R. C. Dye, M. Q. Le, and X. D. Wu, Appl. Phys. Lett. **63**, 1848 (1993); S. R. Folytn, Q. C. Jia, P. N. Arendt, L. Kinder, Y. Fan, and J. F. Smith, 1999 *ibid* **75**, 3692 (1999).

49. In some publications,"δl *pinning*" is often called "$\delta\kappa$ *pinning*"

50. R. Griessen, Hai-Hu Wen, A. J. J. van Dalen, B. Dam, J. Rector, and H. G. Schnack, Phys. Rev. Lett. **72**, 1910 (1994).

Bibliography

- A. Aharoni, *Introduction to the Theory of Ferromagnetism* (Oxford University Press, New York, 2000), 2nd ed.
- N. W. Ashcroft and N. D. Mermin, *Solid State Physics* (Saunders College Publishing, Fort Worth, 1976), college ed.
- R. M. Bozorth, *Ferromagnetism* (IEEE Press, New York, 1978).
- G. Burns, *High Temprature Superconductivity: An Introduction* (Academic Press, New York, 1992).
- W. J. Carr, *AC Loss and Macroscopic Theory of Superconductors* (Gordon and Breach Science Publishers, New York, 2001).
- S. Chikazumi, *Physics of Ferromagnetism* (Oxford University Press, New York, 1997), 2nd ed.
- B. D. Cullity, *Introduction to Magnetic Materials* (Addison-Wesley Publishing, Reading, Massachusetts, 1972).
- C. Kittel, *Introduction to Solid State Physics* (John Wiley and Sons, New York, 1996), 7th ed.
- R. C. O'Handley, *Modern Magnetic Materials: Principles and Applications* (John Wiley and Sons, New York, 2000).

- T. P. Sheahen, *Introduction to High - Temperature Superconductivity*, (Edited by TPS), (Plenum Press, New York, 1994).
- K. D. Sorge, "Magnetic Properties of Nanoparticles Systems of Fe, Co, Ni, and FePt, created by Ion Implantation," (Ph. D. Dissertation August 2002).
- M. Tinkham, *Introduction to Superconductivity* (Dover Publications, Mineola, NY 1996).

Appendix

Appendix A

Publications and Presentations

Publications

1. A. Goyal, S. Kang, K. J. Leonard, P. M. Martin, A. A. Gapud, M. Varela, M. Paranthaman, A. O. Ijaduola, E. D. Specht, J. R. Thompson, D. K. Christen, S. J. Pennycook, and F. A. List, Supercond. Sci. Technol. **18**, 1533 (2005).

2. A. O. Ijaduola, J. R. Thompson, A. Goyal, C. L. H. Thieme, and K. Marken, Physica C **403**, 163 (2004).

3. T. Aytug, M. Paranthaman, J. R. Thompson, A. Goyal, N. Rutter, H. Y. Zhai, A. A. Gapud, A. O. Ijaduola, and D. K. Christen, Appl. Phys. Lett. **83**, 3963 (2003).

4. R. C. Duckworth, J. R. Thompson, M. J. Gouge, J. W. Lue, A. O. Ijaduola, D. Yu, and D. T. Verebelyi, Supercond. Sci. Technol. **16**, 1294 (2003).

Presentations

1. **The Spring 2005 Meeting of the Materials Research Society**, "Development of High-I_c *ex situ* YBCO Coated Conductors: Trends in Thickness Dependence, Grain Boundary Networks, and Vortex Pinning,". R. Feenstra, A. A. Gapud, E. D. Specht, C. Cantoni, A. Ijaduola, J. R. Thompson, D. K. Christen, T. G. Holesinger,

D. M. Feldmann, D. C. Larbalestier, A. Palau, T. Puig, and X. Obradors, San Francisco, CA, March 28 - April 1, 2005.

2. **The Spring 2005 Meeting of the Materials Research Society**, "Columnar Defects Comprised of Self-Aligned Nanodots and Nanorods in YBaCuO on RABiTS," (invited) Sukill Kang, Amit Goyal, Keith J. Leonard, Albert A. Gapud, Maria Varela del Arco, Mariappan Parans Paranthaman, Patrick M. Martin, Anota O. Ijaduola, and James R. Thompson, San Francisco, CA, March 28 - April 1, 2005.

3. **APS 05 March Meeting**, "Critical Currents of $ex-situ$ YBCO Thin Films on "RABiTS" Substrates: Thickness, Field and Temperature Dependencies," A. O. Ijaduola, J. R. Thompson, R. Feenstra, D. K. Christen, and A. A. Gapud, Los Angeles, CA, March 21 - 25 2005.

4. **2005 National Conference of Black Physics Students**, "AC Loss and Thickness Dependence of Critical Currents in Coated conductors," A.O. Ijaduola, J. R. Thompson, R. Feenstra, D. K. Christen, and A. A. Gapud, Chicago, IL, February 3 - 6 2005.

5. **10th International Vortex Workshop**, "Irradiation-free Columnar Defects in YBaCuO-based Coated Conductors on "RABiTS" Substrates," J. R. Thompson, A. Goyal, S. Kang, A. O. Ijaduola, A. A. Gapud, K. Leonard, M. Varela, and D. K. Christen, Mumbai, India, January 9 - 14 2005.

6. **SESAPS 04 Meeting**, "Critical Currents of $ex - situ$ YBCO Thin Films on "RABiTS" Substrates: Thickness, Field and Temperature Dependencies," A.O. Ijaduola, J. R. Thompson, R. Feenstra, D. K. Christen, and A. A. Gapud, Oak Ridge, TN, November 11 - 13 2004.

7. **2004 Japan-US AC Loss Workshop**, "Magnetism and Hysteretic Loss in Ni-based Substrates Materials for "RABiTS" Coated Conductors," J. R. Thompson,

A. O. Ijaduola, A. Goyal, R. C. Duckworth, D. K. Christen, C. L. H. Thieme and K. Marken , Oak Ridge, TN, September 30 - October 1 2004.

8. **APS 04 March Meeting**, "Magnetism and Ferromagnetic Loss in Ni-W Textured Substrates for Coated Conductors," A. O. Ijaduola, J. R. Thompson, A. Goyal, C. L. H. Thieme, and K. Marken, Montreal, Quebec, Canada, March 22 - 25 2004.

9. **2004 AFOSR HTS Coated Conductor Review**, "Magnetism and Hysteretic Loss in Ni-based Substrates Materials and "RABiTS" Coated Conductors," J. R. Thompson, A. O. Ijaduola, A. Goyal, R. C. Duckworth, D. K. Christen, C. L. H. Thieme and K. Marken , St. Petersburg, FL, January 19 - 21 2003.

10. **The Fall 2003 Meeting of the Materials Research Society**, "Electrical and Magnetic Property Characterizations of Cu-RABiTS with conductive Buffer Layers," T. Aytug, M. Paranthaman, J. R. Thompson, A. Goyal, A. A. Gapud, H. Y. Zhai, N. Rutter, A. O. Ijaduola, H. M. Christen, D. K. Christen, and R. E. Ericson, Boston, MA, December 1 - 5 2003.

11. **2003 AFOSR HTS Coated Conductor Review**, "Magnetism and Ferromagnetic Loss in Ni-based Substrates for Coated Conductors," J. R. Thompson, A. O. Ijaduola, A. Goyal, D. K. Christen, and D. M. Kroeger, St. Petersburg, FL, January 22 - 24 2003.

Vita

Anota Oluwatoyin Ijaduola was born in Lagos, Nigeria. After graduating in 1988 from Igbobi Girls' High School in Lagos, she attended Ogun State University, now known as Olabisi Onabanjo Univesity located in Ago-Iwoye, Nigeria from which she graduated with a B.Sc. in Physics in May 1994. She then proceeded for her Masters degree in Physics at the University of Ibadan, Nigeria. During this period, she was selected to participate in the Diploma programme in High Energy Physics at the Abdus Salam International Center for Theoretical Physics in Trieste, Italy. The diploma was awarded to Ms. Ijaduola in September 1997 after which she returned to complete her suspended M.Sc programme at the University of Ibadan.

After obtaining the M.Sc degree in Physics, Ms. Ijaduola enrolled for graduate studies at the University of Illinois at Chicago in the fall of 1999. She earned a MS in Physics in May 2001 and then proceeded for her Ph.D. studies at the University of Tennessee. In August 2002, she joined the research group of James R. Thompson. While at UT, she was awarded the Fowler-Marion fellowship in April 2003. She received the degree of Doctor of Philosophy with a major in Physics in December 2005.

Anota Ijaduola is a member of the American Physical Society and the Physics honour society, Sigma Pi Sigma. She loves to cook and read in her pleasure time.